Characteristics of African Easterly Waves Depicted by ECMWF Reanalyses for 1991–2000

TSING-CHANG CHEN*

Atmospheric Science Program, Department of Geological and Atmospheric Sciences, Iowa State University, Ames, Iowa

(Manuscript received 1 August 2005, in final form 22 March 2006)

ABSTRACT

Several interesting characteristics of African easterly waves (AEWs) were observed and investigated by previous studies: two separate propagation paths, genesis mechanisms, restriction of vertical development, and the interaction with the African easterly jet (AEJ). However, some aspects of these characteristics have been neglected: the contrast of the AEW population along the two propagation paths, the AEW genesis mechanism over the Saharan thermal low and the role played by the low-level North African circulation in this mechanism, the dynamical mechanism restricting the vertical development of AEWs, and the synoptic relationship and interaction between the AEJ and the AEWs along the two propagation paths. The ECMWF reanalyses for the 1991–2000 period supplemented with those of 1979 were analyzed to explore these AEW features. Major findings of this effort are the following:

1) The population of AEWs along the propagation path north of the AEJ (AEW_n) is approximately 2.5 times of that along the propagation path south of the AEJ (AEW_s).
2) The AEW_n geneses primarily occur over the three convergent centers and the southwestward extension of the Saharan thermal low. Underneath the midtropospheric Saharan high, the baroclinic instability of a shallow, low static stability environment, which may be triggered by the intrusion of dry northerlies over central North Africa, leads to the AEW genesis.
3) Continental-scale upward motion along the Saharan thermal low and the cyclonic-shear side of the AEJ maintains positive vortex stretching below the Saharan high and the western part of the Asian monsoon high. These two regions thus form a favorable environment for the development of AEWs within the near-surface troposphere along the Saharan thermal low and the midtroposphere south of the AEJ.
4) The passage of AEW_n (AEW_s) across the coastal zone of West Africa is accompanied by a weak (strong) AEJ and weak (strong) Saharan high. The westward propagation and development/maintenance of the two types of AEWs are achieved through vorticity advection by the AEJ, which is the major AEW–AEJ interaction.

These findings will facilitate the search for AEW dynamics and aid in assessing the impact of AEW activity on North African climate change.

1. Introduction

The general depiction of African easterly wave (AEW) activity was first presented by Carlson (1969a,b). These studies led Burpee (1972) to explore the structure, genesis mechanism, and preferred region of AEW occurrence over North/West Africa. The Global Atmospheric Research Program (GARP) Atlantic Tropical Experiment (GATE) was conducted in 1974. Our understanding of the structure and dynamics of AEWs was enhanced by analyses using GATE observations. Reed (1979) offered an excellent review of several distinct features of AEWs revealed from phase III of GATE. Because GATE was located over the eastern North Atlantic off the West African coast, AEWs have already matured after they travel for some distance from the continent to reach the GATE region. Thus, the AEW characteristics over this region reflect only their mature phase. In contrast, using the First

* Visiting scientist at the National Central University in Taiwan sponsored by a National Science Council chair.

Corresponding author address: Tsing-Chang (Mike) Chen, Atmospheric Science Program, Department of Geological and Atmospheric Sciences, 3010 Agronomy Hall, Iowa State University, Ames, IA 50011.
E-mail: tmchen@iastate.edu

GARP Global Experiment (FGGE) and modern reanalysis data, post-GATE research efforts paid more attention to the AEW activity over the North African continent.

Using surface observations and upper-air soundings for two summers (1968–69), Burpee (1974) identified two AEW propagation paths: one along the Saharan thermal low near 20°N and the other related to the rainy zone close to 10°N. For convenience, let us denote the AEW along the north and south paths as AEW_n and AEW_s, respectively. These two propagation paths were later confirmed by post-GATE studies with the FGGE/post-FGGE data (Nitta and Takayabu 1985; Reed et al. 1988a; Lau and Lau 1990) and with modern reanalyses (e.g., Pytharoulis and Thorncroft 1999; Thorncroft and Hodges 2001; Grist 2002; Grist et al. 2002; Fink et al. 2004). Because of the existence of an easterly maximum along equatorial Africa, Burpee (1972) considered that AEWs were possibly generated by the barotropic–baroclinic instability (Charney and Stern 1962). This instability requires a sign change of the meridional gradient of potential vorticity gradient or negative potential vorticity gradient coupled with a surface maximum gradient of potential temperature. The criterion required by this instability is met by the atmospheric flow over equatorial Africa (e.g., Pytharoulis and Thorncroft 1999; Fink et al. 2004). Solar heating makes the near-surface troposphere over the Saharan thermal low region a low static stability environment. Chang (1993) and Thorncroft and Hoskins (1994a,b) showed that disturbances with AEW characteristics can also be generated by the baroclinic instability of the lower troposphere underneath the Saharan high. The preferred regions of AEW occurrence were also identified by previous studies: 10°W–30°E south of the African easterly jet (AEJ; Burpee 1972; Reed et al. 1988a; Pytharoulis and Thorncroft 1999), and 10°W–5°E north of the jet in the desert region (Reed et al. 1988a; Pytharoulis and Thorncroft 1999).

Two maxima of the 2.9–4.3-day filtered meridional wind variance were displayed by Reed et al. (1988b) on the 9°W latitude–height cross section: one at low levels north of the AEJ and another at the AEJ level south of this jet. Analyzing the 2.5–6-day filtered meridional wind at Dakar, Senegal (north of the AEJ) and Bamako, Mali (south of the AEJ), Pytharoulis and Thorncroft (1999) showed that AEWs attain maximum amplitude in the midtroposphere south of the jet and at low levels north of the jet. It was indicated by previous analyses of the AEW energetics (e.g., Norquist et al. 1977; Fink et al. 2004) and the AEJ instability (e.g., Simmons 1977; Thorncroft and Hoskins 1994a,b; Grist et al. 2002) that AEWs grow at the expense of the AEJ. Nitta and Takayabu (1985) therefore questioned whether the low-level AEWs north and south of the AEJ developed independently. Examining the statistics of their filtered meridional wind at different longitudes, Pytharoulis and Thorncroft (1999) found that AEW activity migrates with the AEJ and that westward propagations of AEW_s and AEW_n are highly correlated.

Findings of these AEW characteristics lead us to raise the following questions:

1) The high correlation between westward-propagating AEW_s and AEW_n may suggest that populations of these two types of AEWs are comparable. Actually, Reed et al. (1988a) observed that the population of AEW_n is larger than AEW_s. Because the time periods of the datasets analyzed in these studies were short, observations of these studies may not be representative. What is the actual population contrast between AEW_s and AEW_n?
2) Two possible genesis mechanisms of AEWs were suggested: the Charney–Stern barotropic–baroclinic instability in the midtroposphere south of the AEJ, and the baroclinic instability in a shallow lower-tropospheric layer with low static stability north of the AEJ. If the population of AEW_n is much larger than that of AEW_s, can the second genesis mechanism of AEWs be a more effective one? Because the AEW_n genesis and development starts at low levels, how does the low-level circulation over North Africa affect this genesis?
3) AEW_ns develop at low levels, while AEW_ss grow in the midtroposphere. Why are vertical developments of both AEW_n and AEW_s restricted in different layers of the troposphere? Can the Saharan high and the western part of the Asian monsoon high hinder the vertical developments of AEW_n and AEW_s, respectively?
4) Because the AEW_n population may be larger than the AEW_s population, what is the relationship between these two different types of AEWs and how do they interact with the AEJ?

During their mature phases, AEWs may reach a horizontal scale of approximately 2000–4000 km. Some of these waves develop from disturbances below 700 mb along the Saharan thermal low (approximately 20°N). To obtain a more accurate depiction of AEWs along this northern path, data should be generated by an assimilation system with a high horizontal resolution, a fine planetary boundary layer, and proper surface initial conditions. The European Centre for Medium-Range Weather Forecasts (ECMWF) reanalyses, which were originally assimilated for 1957–97 and designated

as the ECMWF 40-yr Re-Analysis (ERA-40), and later expanded to cover 1998–2002 (Källberg et al. 2004), meet these special needs; a model with spectral resolution of T159L60, including a well-resolved boundary layer and land surface scheme (van den Hurk et al. 2000), and observations of surface air temperature are used in the ERA-40 data assimilation (Kalnay and Cai 2003). The ERA-40 daily reanalyses for four synoptic times (0000, 0600, 1200, and 1800 UTC) during the summer season [June–September (JJAS)] of a 10-yr (1991–2000) period were analyzed to answer the four questions listed in sections 2–5, respectively. The 1979 summer was part of the FGGE, which had a better coverage of surface observations over North Africa. Because of this, the relationship and interaction between AEWs and the AEJ reported in section 5 was examined using this summer before the other three aspects of AEWs were investigated. In addition to the 10-yr period of 1991–2000, we also included 1979 in the analysis presented in section 5. A summary and some remarks on this study are presented in section 6.

2. Propagation paths of AEWs

Identification of AEWs

As summarized by Fink et al. (2004), three approaches were applied to identify AEWs:

1) *Manual tracking:* Using streamline charts and satellite imageries, Carlson (1969a,b) identified the low-level relatively cloud-free vortex coupled with the upper-level synoptic wave over North Africa. Later, Reed et al. (1988a) described the AEW history in terms of 700-mb trough axes and 850-mb vorticity maxima superimposed on streamline charts and satellite cloud imageries. Most recently, Fink et al. (2004) identified the AEW trough with an *x–t* diagram of meridional wind and located the cyclonic center of AEWs with 2–6-day filtered streamline charts. The filtered vorticity was added in cases without a cyclonic circulation center shown in streamline charts.
2) *Automated tracking*: Thorncroft and Rowell (1998) designed an automated tracking procedure to identify AEWs simulated by a general circulation model: the number of disturbances passing selected points with amplitude of the 2.5–5-day filtered 850-mb meridional wind larger than 2.5, 5, and 7.5 m s^{-1}. Later, the automated tracking approach of Hodges (1995) was adopted by Thorncroft and Hodges (2001) to track AEWs with their vorticity maxima exceeding a threshold value of 0.5×10^{-5} s^{-1}, life spans larger than 2 days, and westward motion over a distance larger than 10° longitude.
3) *Statistical method*: Because of limited upper-air observations, simple statistical analyses including power spectra, composite charts, and kinetic energy of horizontal winds were used to identify the signal, spatial structure, and propagation paths of AEWs (e.g., Burpee 1972, 1974; Pytharoulis and Thorncroft 1999, and others). Findings with radiosonde observations were confirmed with the reanalysis data and more sophisticated statistical schemes, including spectral and composite analyses, the lagged correlation pattern, extended empirical orthogonal function, and rotated EOF analyses (e.g., Lau and Lau 1990).

The automated and statistical tracking methods are economic and objective in depicting AEW characteristics. However, these methods are hampered by choosing thresholds or selecting criteria in determining AEW. The manual tracking approach is more realistic in locating the AEW genesis and quantitatively measuring the AEW population of the two propagation paths. Using the interactive technique provided by the Grid Analysis and Display System, we are able to track locations of AEW with a high accuracy. Even with this technique advantage, it is not possible to be completely free of human errors. Furthermore, manual tracking is always a time-consuming exercise. However, in order to answer some concerns posed in the introduction, the manual tracking approach supplemented with procedures introduced by Fink et al. (2004) is adopted in the current study. These supplemental procedures include the *x–t* diagram of 600-mb meridional wind and spatially Fourier-filtered streamfunction. Details of the approach used in this study are presented below.

1) BACKTRACKING

AEWs become mature when they reach the west coast of Africa. Thus, the maximum AEW amplitudes west of this coast usually appear at the midtropospheric AEJ level (e.g., Reed et al. 1988b). Even without a special criterion, AEW troughs can be easily identified on the 600-mb streamline charts with vorticity isopleths superimposed, as done by Reed et al. (1988a) and Fink et al. (2004), with the 700-mb streamline charts and 850-mb vorticity. Longitudinal locations of these AEW troughs can be further confirmed by the once-daily National Oceanic and Atmospheric Administration outgoing longwave radiation data. After AEW troughs were identified near the coast of West Africa, the backtracking procedure was applied to trace propagation paths of AEWs. An advantage of this approach is to reduce

difficulty in identifying AEWs over the continent. A disadvantage is that some weak disturbances may not be counted if they cannot reach the West African coast. If the forward-tracking approach was adopted, we may face some uncertainty in determining genesis locations of AEWs, particularly AEW_ns, and their ensuing development experienced by previous studies (e.g., Reed et al. 1988a; Fink et al. 2004). Therefore, additional constraints were added on the backtracking of the already identified AEWs within the continent in determining genesis locations of both AEW_n and AEW_s.

(i) Northern path

1) The 925-mb vorticity maximum of an identified AEW inside North Africa is traced to its genesis location, which is always north of the AEJ.
2) The sea level pressure around the AEW_n genesis location is smaller than or equal to 1010 mb.
3) The AEW genesis is generally accompanied by the convergence of the Harmattan (surface northerlies of North Africa) and the surface monsoon southerlies.
4) Before being able to be transported by the AEJ, the newly generated AEW_ns move westward underneath the midtropospheric Saharan anticyclone.

(ii) Southern path

1) The 600-mb vorticity maximum of an identified AEW is traced to the location where a cyclonic perturbation appears the first time south of the AEJ and along the southern rim of the Saharan high. During its genesis phase, an AEW_s may not exhibit a noticeable perturbation in surface pressure and 925-mb vorticity.
2) The cyclonic low of the 2–7-day filtered streamline is added in locating the AEW_s perturbation if it is not well defined by the 600-mb streamline chart superimposed with vorticity. The Butterworth bandpass filter (Murakami 1979) was adopted in this study to prepare the filtered field variables.

2) PROPAGATION PATHS

(i) North of the AEJ

As inferred from the low sea level pressure and convergence of 925-mb streamlines shown in Figs. 1c,f, the merger of the Harmattan and the monsoon southwesterlies forms a low-level convergence zone along the Saharan thermal low (the zonally elongated white-colored region). Locations (dots) of the AEW_n vortices at 925 mb every 6 h are distributed primarily along the Saharan thermal low (Fig. 1c). Two interesting features of AEW_n locations are revealed. First, four clusters of AEW_ns are located over the convergent centers between the west coast and 10°W, 10°W–5°E, 10°–20°E, and 25°–30°E. This coincidence suggests that the AEW_n genesis is closely related to the circulation structure of the environment around these centers, which will be addressed in section 3. Second, it is inferred from the spatial relationship between AEW_n locations and the Saharan thermal low that the AEW_ns are transported westward by the Harmattan through the meridional advection of planetary vorticity.

The propagation path of AEW_n turns southwestward across the coast of West Africa into the eastern North Atlantic (Fig. 1c). This direction change of the AEW_n propagation was observed by Reed et al. (1988a) and Pytharoulis and Thorncroft (1999). As indicated by maximum RMS(v') at 5°W (where v' is the 2–7-day filtered meridional wind) near the surface around 20°N in Fig. 2a, AEW_ns are shallow perturbations during their initial phase. The spatial separation between maximum RMS(v') and the AEJ does not suggest a strong interaction between AEW_ns and this midtropospheric jet. However, when AEW_ns move close to the coast of West Africa, these waves are transported by northeasterlies of the North Atlantic anticyclone along the southwestward extension of the Saharan thermal low (Fig. 1c). On the other hand, it is inferred from maximum RMS(v') at 20°W (Fig. 2b) that the eastern North Atlantic ITCZ may facilitate the midtropospheric development of AEW_ns when they reach that point.

Except for the monsoon southwesterlies along the Guinea coast and the Harmattan over central North Africa in the lower troposphere (Figs. 1c,f), the basic elements of the North African summer circulation are depicted by the latitude–height cross section of streamfunction and zonal wind at 5°E [(ψ, u)(5°E)] in Fig. 3. The North African summer circulation in the lower half of the troposphere consists of the midtropospheric Saharan high and the low-level Saharan thermal low (Cook 1999; Chen 2005). The vertical structure of this circulation resembles a monsoon circulation (Chen 2003). Aloft over the midtropospheric Saharan high exists the western part of the Asian monsoon high (Fig. 1a). Around the southern rim of this monsoon high is the tropical easterly jet (TEJ; thick, solid line in Figs. 1a,d). Because this jet is located farther south of the AEW_n propagation path, the large spatial distance does not suggest any relation between them. This assertion is echoed by the RMS(v') distribution in Fig. 2a where the RMS(v') maximum is located north of the AEJ and underneath the Saharan anticyclone. Evidently, AEW_n activity is independent of the Asian monsoon high.

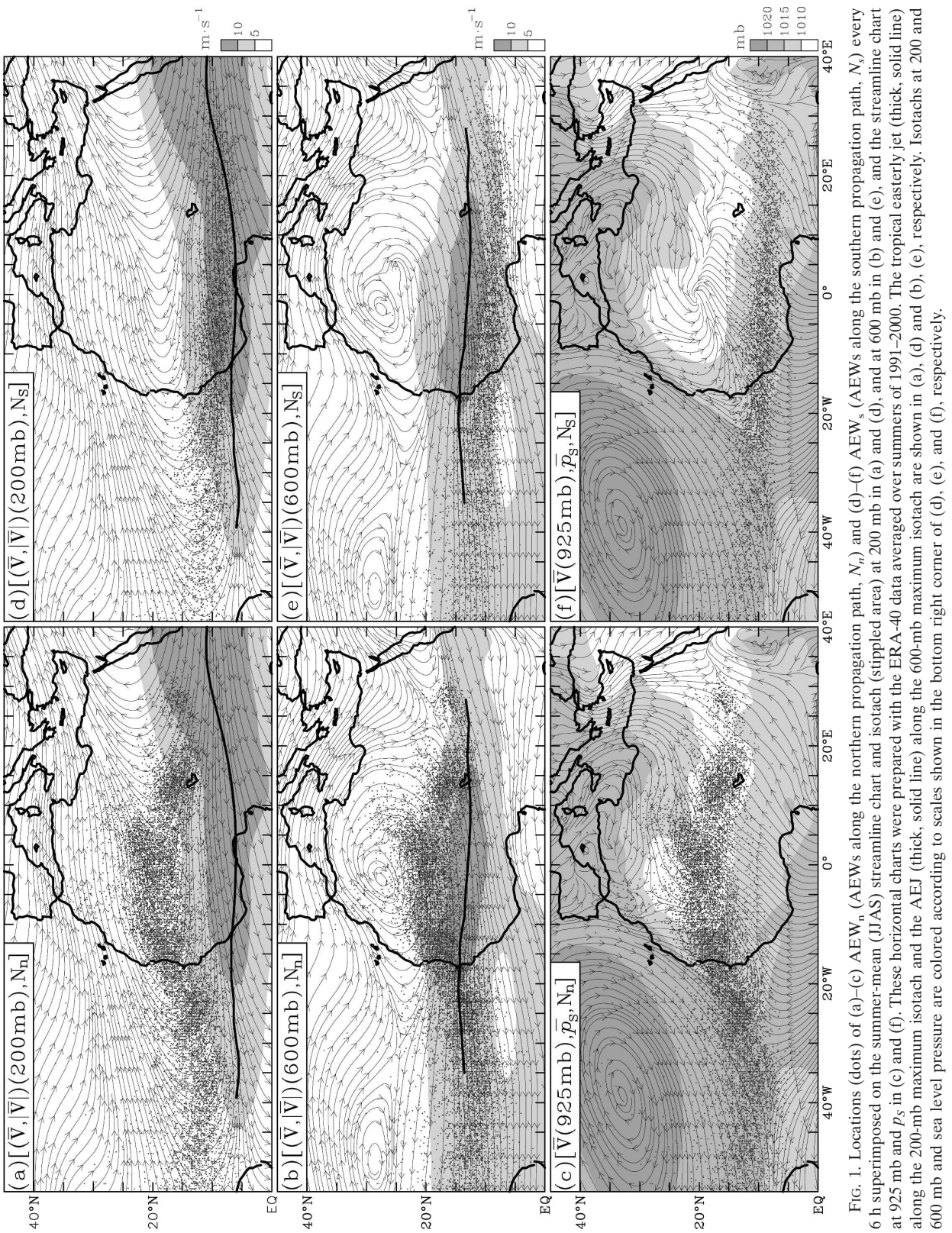

FIG. 1. Locations (dots) of (a)–(c) AEW_n (AEWs along the northern propagation path, N_n) and (d)–(f) AEW_s (AEWs along the southern propagation path, N_s) every 6 h superimposed on the summer-mean (JJAS) streamline chart and isotach (stippled area) at 200 mb in (a) and (d), and at 600 mb in (b) and (e), and the streamline chart at 925 mb and p_S in (c) and (f). These horizontal charts were prepared with the ERA-40 data averaged over summers of 1991–2000. The tropical easterly jet (thick, solid line) along the 200-mb maximum isotach and the AEJ (thick, solid line) along the 600-mb maximum isotach are shown in (a), (d) and (b), (e), respectively. Isotachs at 200 and 600 mb and sea level pressure are colored according to scales shown in the bottom right corner of (d), (e), and (f), respectively.

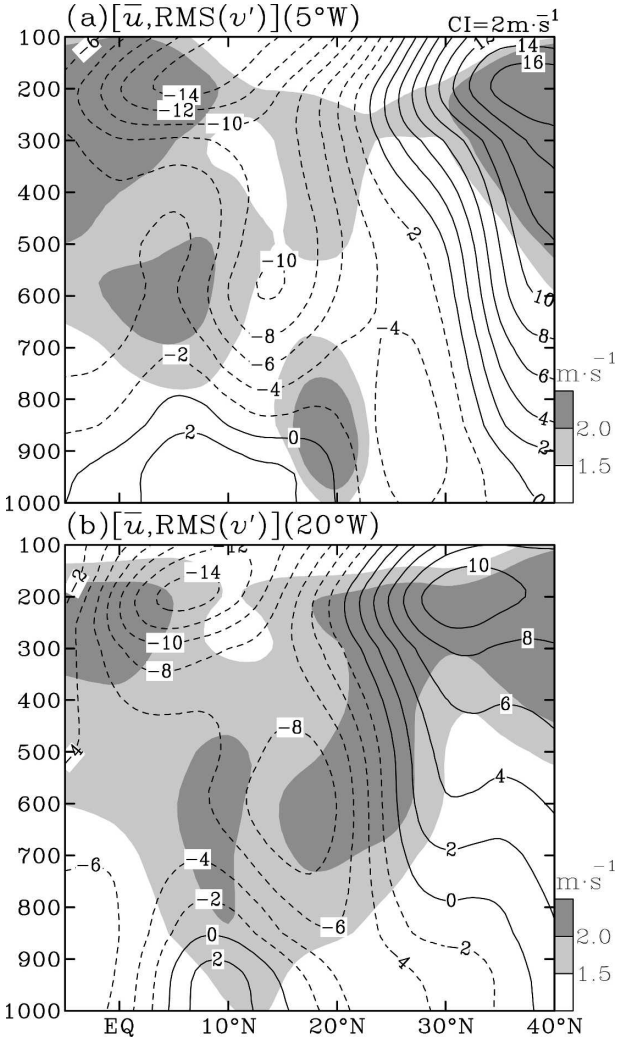

FIG. 2. Summer-mean (JJAS) RMS values of the 2–7-day filtered meridional wind RMS(v') (shaded areas) superimposed on zonal flow $\bar{u}$ (contoured) at (a) 5° and (b) 20°W over the period of 1991–2000. The contour interval of $\bar{u}$(5°W) is shown at the right top of (a), while the contour interval of RMS(v') is shown by the scale in the bottom right side of both (a) and (b).

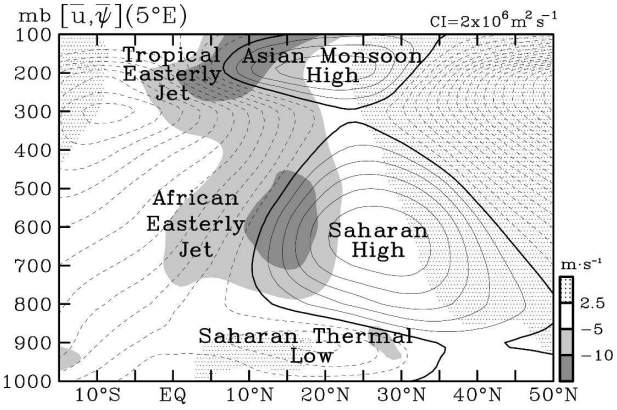

FIG. 3. Major elements of the North African summer circulation indicated in terms of the latitude–height cross section of summer-mean ($\bar{u}$, $\bar{\psi}$) at 5°E for the period of 1979–2000 (Fig. 2a of Chen 2005). The contour interval of $\bar{\psi}$(5°E) is 2×10^6 m^2 s^{-1}, while that of $\bar{u}$(5°E) is shown by the scale shown in the bottom-right-hand corner.

(ii) South of the AEJ

The AEJ is located around the southern rim of the Saharan anticyclone (Fig. 1e). Dynamically, the cyclonic shear and vertical shear south and below this jet (Fig. 2a), respectively, make the region south of the AEJ a preferred environment for cyclogenesis (Burpee 1972). This argument is supported by the maximum RMS(v') at 5°W located south of the AEJ core at 600 mb (Fig. 2a). Locations of AEW_s superimposed on sea level pressure p_S (Fig. 1f) indicate that these waves generally exist south of the Saharan thermal low and rarely move northward across the AEJ (Fig. 1e). Two completely separate propagation paths of AEWs emerge from locations of AEW_ns (Fig. 1b) and AEW_ss (Fig. 1e) over the North African continent, although these two paths eventually merge in the Atlantic.

Projecting locations of all AEW_ss on the 200-mb streamline chart (Fig. 1d), one may find that almost all AEW_ss are located north of the TEJ, which appears along the coast of Guinea. Not only is the anticyclonic shear north of the TEJ not conducive to cyclogenesis, the Asian monsoon high may also hinder the vertical development of AEW_ss. This inference is supported by the latitude–height cross section of RMS(v') against zonal flows at different longitudes shown in Fig. 2. These arguments do not seem to suggest any possible link between AEW_ss and the TEJ.

In addition to the existence of two separate propagation paths of AEWs, a concern posed in the introduction was the population contrast between these two paths. Even without precise number counts of both AEW_ns and AEW_ss, location distributions of AEW_ns (Figs. 1a–c) and AEW_ss (Figs. 1d–f) indicate that the former has a much larger population than the latter. As shown in Fig. 4, total AEWs identified in this study over a period of 10 yr is 428 including 302 AEW_ns and 126 AEW_ss. The mean occurrence frequency of AEWs every summer (JJAS) is approximately 43, which is somewhat smaller than Avila and Pasch's (1992) observation of 59 for May–October 1991. The difference of the AEW populations between these two studies may be due to the inclusion of these two extra months by the latter study. The AEW_s group contributes only 29% of the AEW population, but it is important to West African rainfall. In contrast, the AEW_n group, which constitutes the majority of the AEW population, has not

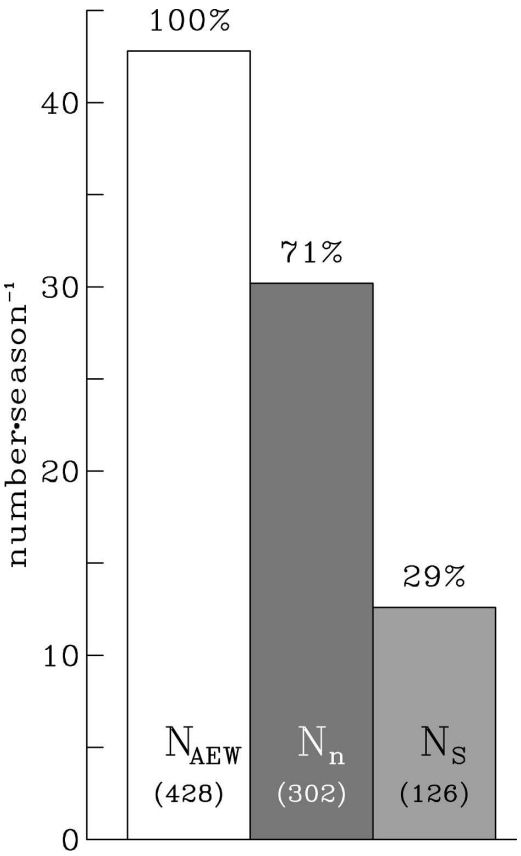

FIG. 4. The AEW population (N_A) contributed by AEW_n (N_n), and AEW_s (N_s) during JJAS for the 1991–2000 period.

yet attracted much attention. Approximately, one-half of the Atlantic tropical cyclones reaching the U.S. coast developed from the AEWs (Landsea 1993). Following the back tracking approach presented in section 2a(1), we found that the AEW_ns contribute not only more to the population of AEWs, but also more to the number of Atlantic tropical cyclones (~65%) than the AEW_ss (based on results of our preliminary analysis). In view of the contribution of AEW_ns to Altantic tropical cyclones, more research effort should be dedicated to understanding the AEW_n dynamics and its impact on the North Atlantic weather system.

3. Genesis mechanisms

a. Mechanisms

The Charney–Stern instability (Charney and Stern 1962) was suggested by Burpee (1972) as the AEW_s genesis mechanism. Numerous studies (e.g., Rennick 1976; Mass 1979; Kwon 1989; Thorncroft and Hoskins 1994a,b) were made to analytically and numerically test this mechanism. Because this mechanism is only applicable to AEW_ss, a smaller population of AEWs south of the AEJ, the majority of AEWs north of the AEJ must be generated by a mechanism different from Burpee's. It was suggested by Chang (1993) and Thorncroft (1995) that this mechanism is the baroclinic instability of a shallow low static stability flow underneath the midtropospheric Saharan high. For convenience, this mechanism is designated hereafter as the Chang–Thorncroft (C–T) baroclinic instability. Eady (1949) showed that the stabilizing effect of static stability results in a short-wave cutoff in the baroclinic instability. The decrease of static stability reduces the wavelength of this cutoff short wave. When static stability vanishes, a so-called ultraviolet catastrophe of instability may occur as long as a given vertical shear (regardless of how small it is; Fjortoft 1950; Arnason 1963) exists. Although the basic flow in Chang's model is different from Eady's (1949) linear vertical shear, the low static stability in Chang's model should have the same effect in the Eady model to reduce the cutoff wavelength. This argument is supported well by our observation (presented later) that the scale of AEW_n is small during its genesis stage.

As revealed from the latitude–height cross section of potential temperature $\overline{\theta}$ (thick, solid line), Ertel potential vorticity $\overline{Q}$ (thin, dashed line), and zonal wind $\overline{u}$ (thin, solid line) at 5°E (Fig. 5a), a reversal of $\overline{Q}_y$ occurs south of the AEJ and $\overline{Q}_y < 0$ appears underneath the AEJ (Charney and Stern 1962) coupled with $\overline{\theta}_y > 0$ near the surface (Thorncroft and Hoskins 1994a). Note that $(\,)_y \equiv \partial(\,)/\partial y$. Evidently, the AEJ satisfies the barotropic–baroclinic instability criterion. On the other hand, it was confirmed by Pytharoulis and Thorncroft (1999) that the environment with low static stability and strong meridional temperature gradient north of the AEJ is a favorable region for the development of AEW disturbances. As shown in Fig. 5b, these requirements are satisfied by the $\overline{\theta}$ (thick, solid line) distribution in the troposphere (below 600 mb) around 20°N (the Saharan thermal low). The environment of low static stability and large meridional thermal gradient may not always warrant the genesis of a synoptic perturbation. However, the low-level convergence formed by the monsoon southwesterlies and the Harmattan induces upward vertical motion along the thermal low (shaded areas in Fig. 5b). Therefore, the genesis of a synoptic disturbance by the C–T baroclinic instability may be triggered by the intrusion of the Harmattan into the low static stability environment. Apparently, the AEW_n genesis is caused by a mechanism different from the AEW_s genesis.

Surface temperatures θ_S over North Africa undergo a pronounced diurnal variation. As revealed from the latitude–height cross section of $\tilde{\theta}$ (diurnal amplitude of

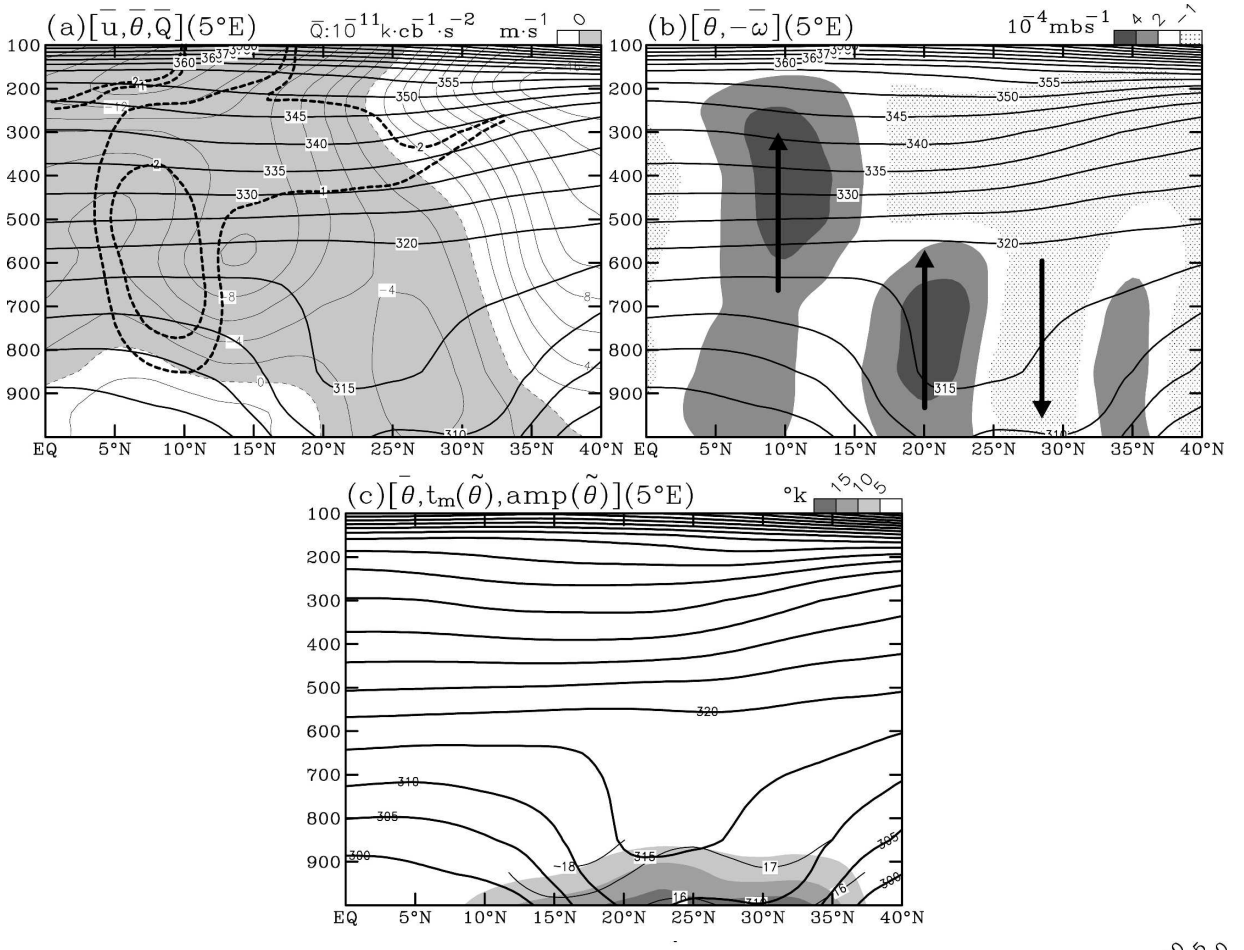

FIG. 5. The 10-yr (1991–2000) averaged latitude–height cross sections of various August monthly-mean variables at 5°E: (a) $\overline{u}$ (zonal flow; thin, solid line), $\overline{\theta}$ (potential temperature; thick, solid line), and $\overline{Q}$ (Ertel potential vorticity; thick, dashed line); (b) $\overline{\theta}$ and $-\overline{\omega}$ (vertical motion; shaded areas); (c) $\overline{\theta}$, t_m (synoptic time of the maximum θ during the day; thin, solid lines near the bottom), and amplitude of θ diurnal variation ($\tilde{\theta}$; shaded areas); and (d) mean sea level pressure ($\overline{p}_S$; shaded areas) and $\tilde{\theta}$ at the surface ($\tilde{\theta}_S$). Contour intervals of the following variables are shown on the top of the individual panels: $\overline{u}$(5°E) and $\overline{Q}$(5°E) in (a), $-\overline{\omega}$(5°E) in (b), Amp($\tilde{\theta}$) in (c), and $\overline{p}_S$ in (d). Note that Amp( ) ≡ amplitude of variable ( ).

θ) and the local time of maximum $\tilde{\theta}$ at 5°E in Fig. 5c, the maximum amplitude of $\tilde{\theta}$ (>15 K shaded area) and maximum temperature appears at 1600–1800 UTC (thin, solid line). The horizontal distribution of $\tilde{\theta}_S$ (amplitude of θ_S) is displayed in Fig. 5d. The static stability ($\partial\theta/\partial p$) near the surface should exhibit a coherent diurnal variation with θ_S. Consequently, the occurrence of AEW_n genesis caused by the C–T baroclinic instability may have a timing preference when the static stability reaches its minimum in late afternoon. As shown in Fig. 6b, the seasonal-mean AEW_s genesis does not exhibit any timing preference. In contrast, the AEW_n genesis (Fig. 6a) reaches its maximum occurrence at 1800 UTC when the near-surface atmosphere becomes statically neutral or weakly unstable. It is easier to reach this condition north of the Saharan thermal low, because amplitude of $\tilde{\theta}$ is larger in this region (Fig. 5d). Depending solely on static stability, the majority of this genesis may occur over the region north of the Saharan thermal low. As will be shown in section 3b, this is not the case. If the C–T baroclinic instability (triggered by the upward motion in response to the intrusion of the Harmattan) is the mechanism responsible for the AEW_n genesis, the majority of this genesis should take place over the region where the upward motion in the lower troposphere is significant along the Saharan thermal low (Fig. 5b). However, this mechanism has not yet been tested against any observed AEW_n genesis. To search for genesis mechanisms of all identified AEWs across the coast of West Africa, some extra constraints are added on two different types of instabilities.

1) AEW_S GENESIS

1) In the southern flank of the AEJ and around the southern rim of the Saharan high, a positive ζ(600 mb) center accompanying the 600-mb perturbation is identified for first time on the 600-mb streamline chart. At this stage, this 600-mb perturbation is not coupled with a noticeable perturbation perceivable at the surface.
2) Positive 600-mb vorticity tendency [ζ_t(600 mb) > 0] appears ahead of the identified perturbation.

2) AEW_N GENESIS

1) At any one of four synoptic times (0000, 0600, 1200, and 1800 UTC), a surface perturbation is identified with the following meteorological conditions: $\partial\theta$(925 mb)/$\partial p \leq 0$ (statically neutral or near unstable), $-\omega$(925 mb) > 0 (upward motion) caused by the convergence between the monsoon southwesterlies and the Harmattan, and $q \leq 5$ g kg^{-1} (dry) near the surface. No corresponding perturbation can be observed above 925 mb.

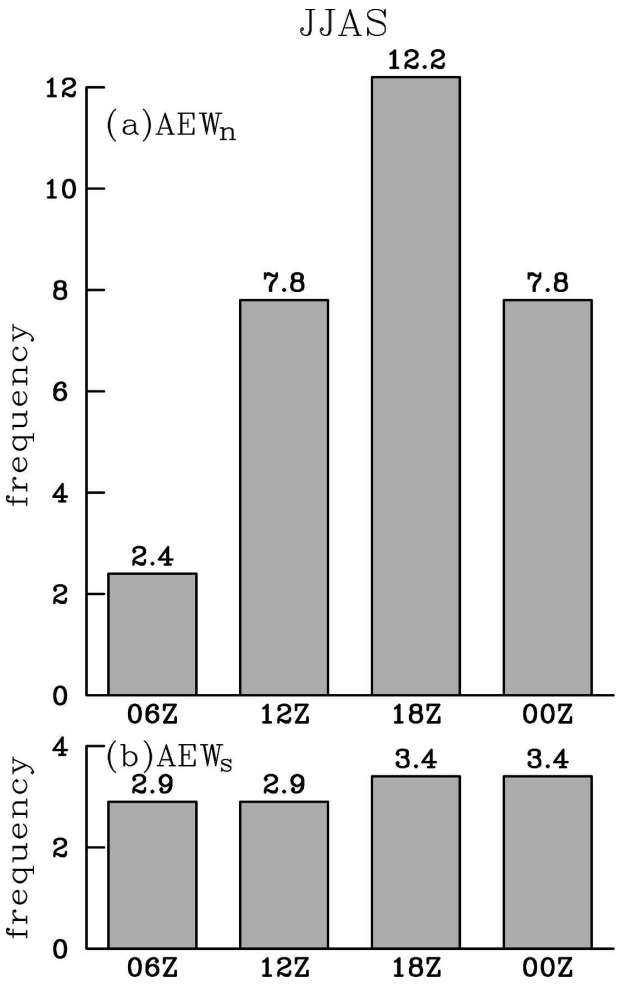

FIG. 6. Summer-mean genesis frequency of (a) AEW_n and (b) AEW_s at four synoptic times (0600, 1200, 1800, and 0000 UTC) averaged for the period of 1991–2000.

2) The identified perturbation is accompanied by a positive ζ(925 mb) center and positive vorticity tendency, ζ_t(925 mb) [$\sim -f\nabla \cdot \mathbf{V}$(925 mb)] > 0, as shown with the 925-mb streamline chart.
3) The p_S (surface pressure) of the surface perturbation ≤1010 mb and surface $\theta_y > 0$ south of this perturbation.

AEW cases used to illustrate the two genesis mechanisms are given in the appendix.

b. Preferred genesis region

The three surface convergent centers along the Saharan thermal low and the southwestward extension of this thermal low (Figs. 1c,f) are coupled with well-organized upward motion (Fig. 7a). Based on the hypothesized AEW_n genesis mechanism, these convergent centers should be the preferred areas of AEW_n

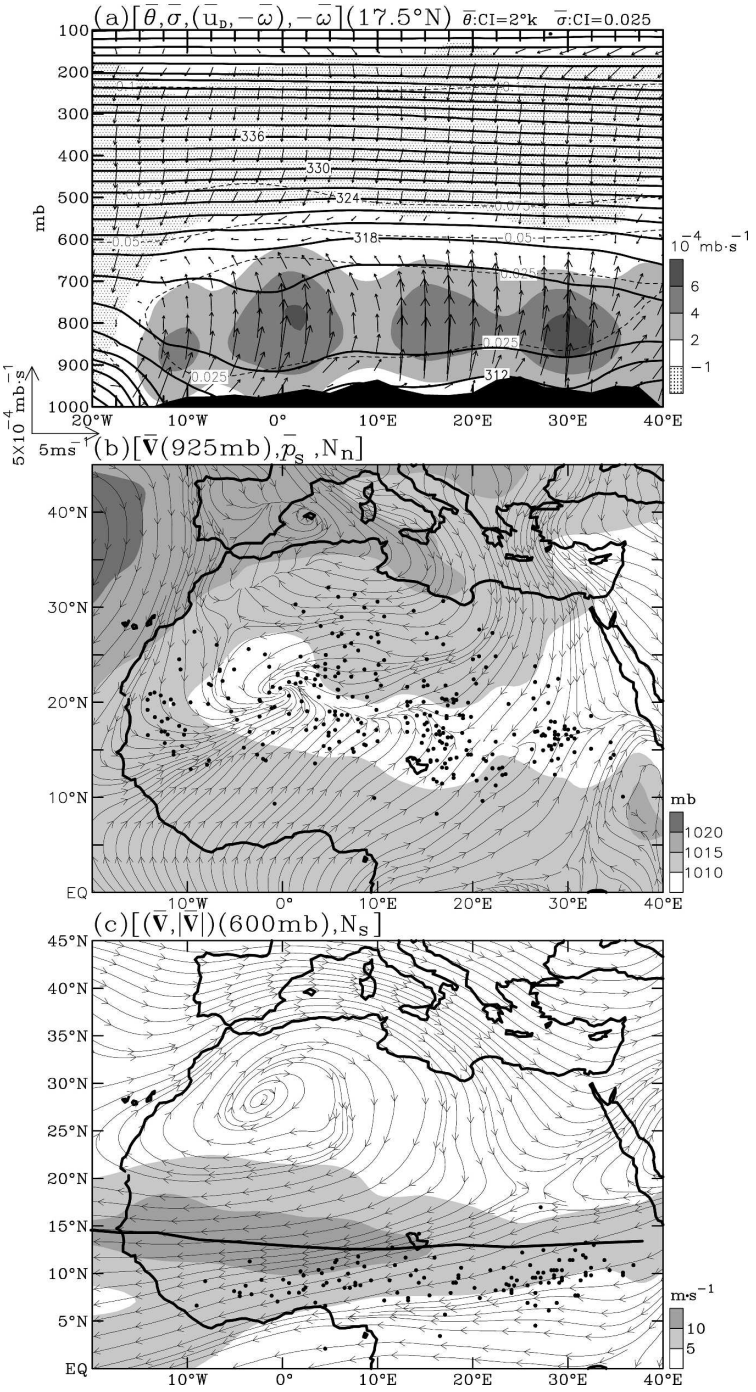

FIG. 7. (a) Longitude–height cross section of summer-mean $\bar{\theta}$ (thick, solid lines), $\bar{\sigma}$ (static stability; thin, dashed lines), ($\bar{u}_D$, $-\omega$) (east–west circulation; $\bar{u}_D$ is zonal component of divergent wind), and $-\omega$ (shaded areas) at 17.5°N to cover three surface convergent centers of North Africa; (b) AEW_n genesis locations (dots) superimposed on summer-mean 925-mb streamlines and sea level pressure (shaded area); and (c) AEW_s genesis locations (dots) superimposed on 600-mb streamlines, isotach (shaded area), and the AEJ core (thick solid line). All summer-mean field variables cover the 1991–2000 period. Contour intervals of $\bar{\theta}$ and $\bar{\sigma}$ are shown at the top right in (a), and $-\bar{\omega}$, $\bar{p}_S$, and isotachs [$|\bar{\mathbf{V}}|$(600 mb)] are shown in the bottom-right-hand side of (a)–(c), respectively.

genesis. As expected, four clusters of identified AEW_n genesis locations (dots) shown in Fig. 7b are overlapped with the Saharan near-surface convergent centers and the southwest thermal low extension. Reed et al. (1988a) observed one preferred region of AEW development bounded by (18°–25°N, 10°W–5°E) over the Sahara downwind of the Hoggar Mountains. Using the distribution of AEW kinetic energy, Pytharoulis and Thorncroft (1999) identified a region with energy larger than 2 $m^2\ s^{-2}$ over the 0°–5°E sub-Saharan baroclinic zone at 950 mb. These observed regions agree with the AEW_n genesis region over the western Sahara. The other three AEW_n genesis regions were not previously recognized.

The AEW_s genesis takes place in the baroclinic zone south of the AEJ by the barotropic–baroclinic instability in tropical Africa (Fig. 7c): these AEW_s genesis locations (dots) are farther south of the Saharan thermal low (Fig. 7b) and extend all the way to 30°E. The western part of this AEW_s genesis region is consistent with Reed et al's (1988a) preferred region of AEW development with the climatological rainy zone over (8°–15°N, 0°–10°E) and Pytharoulis and Thorncroft's (1999) large kinetic energy region of AEW at about 10°–15°E of this rainy area. Although located south of the AEJ (thick, solid line in Fig. 7c) and the Saharan high, the AEW_s geneses occur north of the TEJ (Fig. 1).

4. Limit of the AEW vertical development

As indicated by the RMS(v') distribution (Fig. 2a), AEW_ns and AEW_ss only exist in the lower and midtroposphere, respectively. Why is there such a clear contrast in the vertical development of AEWs along two different propagation paths? The AEW_ns are generated near the surface of the Saharan thermal low north of the AEJ, while the AEW_ss originate in the midtroposphere south of the AEJ. Is the difference in the vertical development between AEW_ns and AEW_ss attributed to the difference in the elevation of their geneses? Otherwise, can the vertical structure of the North African summer circulation embedded with AEWs have any effect on the vertical development of AEW_ns and AEW_ss? The comparison between the RMS(v') distribution at 5°W (Fig. 2a) and the ψ(5°E) cross section (Fig. 3) suggests that the vertical developments of AEW_ns and AEW_ss are limited by the Saharan and Asian monsoon high, respectively. How do these two upper-level anticyclones affect these vertical developments?

The latitude–height cross section of ψ(5°E) superimposed with the meridional circulation is shown in Fig. 8b. Upward motion over the Saharan thermal low is confined to the lower troposphere by the Saharan anticyclone, while the upward branch of the Hadley circulation in the Tropics is limited by the western part of the Asian monsoon high. The contrast of vertical motions between these two latitudinal zones can be illustrated more clearly with (ψ, $-\omega$) at 20°N (Fig. 8a) and at 10°N (Fig. 8c). The development of synoptic disturbances can be facilitated by upward motion of the large-scale environmental circulation. In view of constraints exerted by the two upper-air anticyclones on the upward motion over the Sahara and tropical West Africa along the Guinea coast, it is expected that vertical developments of AEW_ns and AEW_ss are hindered by the Saharan and Asian monsoon highs, respectively.

The vertical structure of a monsoon circulation is characterized by a phase reversal with a monsoon low in the lower troposphere overlaid by a monsoon anticyclone in the upper troposphere. This vertical structure is well explained by the Sverdrup vorticity balance, a balance between the meridional advection of planetary vorticity advection and vortex stretching (Chen 2003). Because the core speeds of the TEJ and AEJ may reach 25 and 13 $m\ s^{-1}$, respectively, horizontal advection of relative vorticity ζ by these jets is not negligible. However, this dynamic process works coherently with the meridional advection of planetary vorticity f to move perturbations westward. The inclusion of this horizontal advection of relative vorticity by strong easterlies in low latitudes does not change the Sverdrup dynamics. Therefore, the dynamics of the summer tropical circulation may be expressed by the following vorticity equation:

$$0 \simeq \left(-\overline{u}_Z \frac{\partial \overline{\zeta}}{\partial x} - \overline{v}\beta \right) + f \frac{\partial \overline{\omega}}{\partial p}, \tag{1}$$

where the overbar indicates long-term summer-mean value. Here u_z, v, β, and ω are the zonally averaged zonal velocity, meridional wind, meridional gradient of $f\ (=2\Omega \sin\varphi)$, and p velocity, respectively. In the Tropics, thermal advection is generally much weaker than diabatic heating in maintaining vertical motion (e.g., Chen and Baker 1986). Below the Saharan anticyclone, upward motion in the lower troposphere over North Africa is primarily maintained by the Saharan thermal-low heating. Above this anticyclone, downward motion is caused by radiative cooling (Chen 2005). Along the rainy zone of tropical Africa, upward motion underneath the Asian monsoon high is driven by latent heat released by tropical deep cumulus convection. With the difference in vertical motion ($-\omega$) between 20° and 10°N (Fig. 8), positive vortex stretching is likely to appear only in the lower troposphere underneath the Sa-

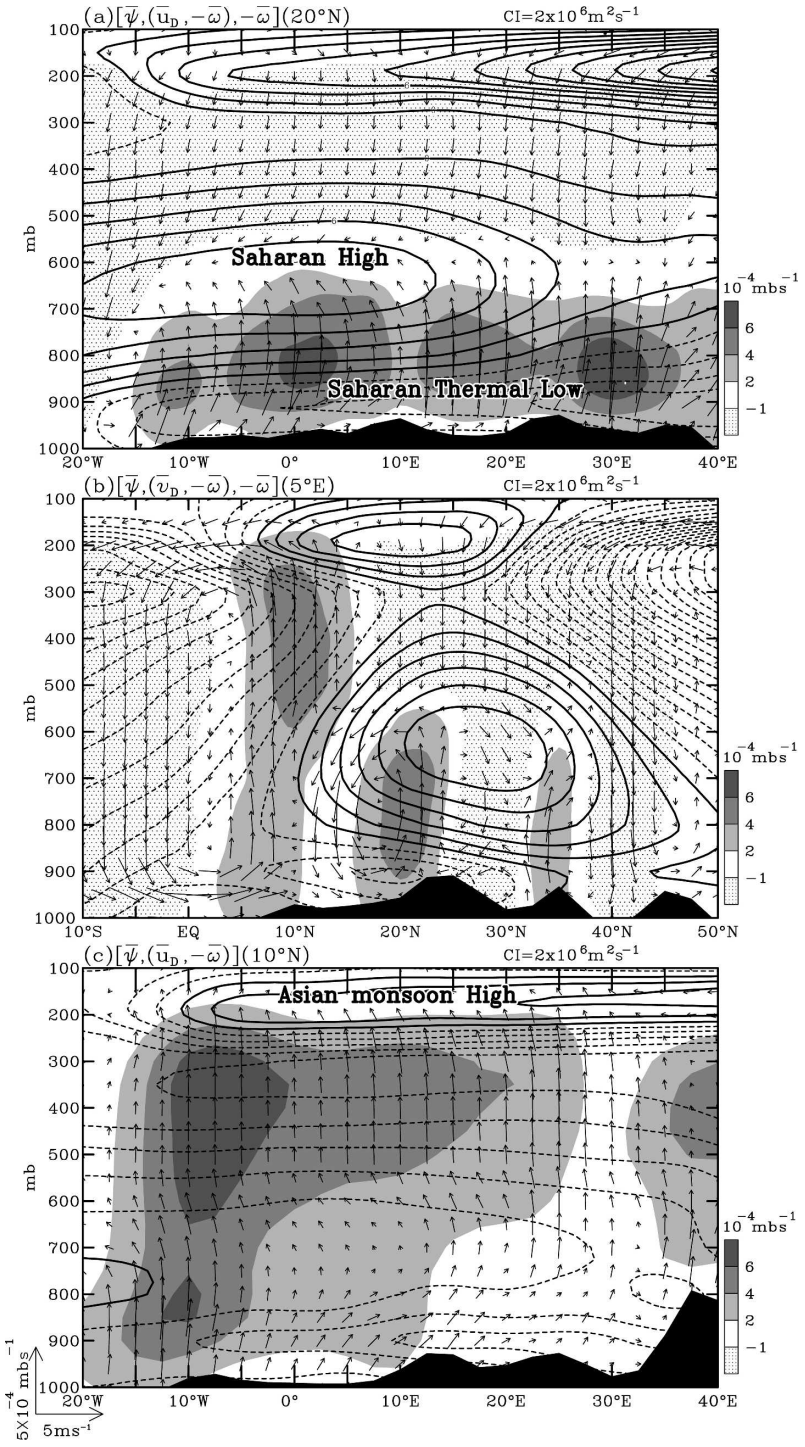

FIG. 8. (a) Longitude–height cross section of $\overline{\psi}$ (contours) and east–west circulation ($\overline{u}_D$, $-\overline{\omega}$) at 20°N superimposed with vertical motion ($-\overline{\omega}$; stippled area), (b) latitude–height cross section of $\overline{\psi}$ and meridional secondary circulation ($\overline{v}_D$, $-\overline{\omega}$) at 5°E superimposed with vertical motion ($-\overline{\omega}$; stippled area), and (c) same as (a) but for 10°N. All variables shown in these cross sections are the summer-mean fields for 1991–2000. The contour interval of $\overline{\psi}$ is 2×10^6 m^2 s^{-1} and the contour interval of $-\overline{\omega}$ is shown by the scale in the bottom-right-hand corner of (a)–(c). The east–west circulation is portrayed with vectors that can be measured by the scale shown in the bottom-left-hand corner of (c).

haran high and in the midtroposphere below the Asian monsoon high, respectively. This inference is confirmed by the opposite vertical differentiation of vortex stretching between 20° and 10°N in Fig. 9.

At 20°N underneath the Saharan high, it is revealed from Figs. 9a,b that strong positive vortex stretching along the Saharan thermal low forms an environment conducive to AEW_n genesis. In contrast, strong negative vortex stretching associated with the midtropospheric Saharan high hinders the development of AEW_n. This vertical differentiation of vortex stretching embedded in the North African summer circulation consequently confines the vertical development of AEW_n below the Saharan high. For the tropical region south of the AEJ, vortex stretching (displayed in Figs. 9b,c) should be counterbalanced by horizontal vorticity advection (confirmed by our diagnosis, but not shown). Based on the vorticity budget, vortex stretching of the environmental flow may not be directly involved with the development of AEW_ss, but supplies vorticity in developing them through the redistribution of vorticity by horizontal advection. In other words, the environmental vorticity, which is generated by vortex stretching, is consumed by horizontal advection through the interaction between the AEW_s perturbations and the environmental flow. This interaction is equivalent to the barotropic energy conversion illustrated by previous studies (e.g., Norquist et al. 1977). For the tropical region south of the AEJ, the midtropospheric positive vortex stretching underneath the Asian monsoon high provides a preferred area not only for the AEW_ss genesis, but also for their development. On the other hand, the strong vortex compression associated with the Asian monsoon high prevents the vertical development of AEW_ss generated in the midtroposphere. Although vortex stretching is weak in the lower troposphere near the surface, its negative values are not helpful in developing AEW_s. Under these circumstances, the AEW_ss' development is restricted within the midtropospheric layer.

The vertical differentiation of vortex stretching in the North African summer circulation forms two preferred paths of the AEW westward propagation: one for AEW_ns in the lower troposphere along the Saharan thermal low and the other for AEW_ss along the midtroposphere south of the AEJ. To substantiate this argument, let us use the RMS values of the 2–7-day filtered vorticity RMS(ζ') as an indicator of AEWs and superimpose them on vortex stretching (contoured) of the environmental flow at 925 and 600 mb in Fig. 10. The coincidence of positive environmental vortex stretching and maximum values of RMS(ζ') supports our argument concerning the two AEW propagation paths.

5. Interaction between the AEJ and AEWs

It was suggested by Burpee (1972) that the growth of AEWs is energetically supported by the AEJ through the AEW–AEJ interaction. This interaction was examined by numerous studies (e.g., Norquist et al. 1977 and many others) in terms of baroclinic and barotropic energy conversions in the Lorenz (1955) energy cycle. Although, the AEJ appears to be zonally oriented in the long-term mean fields (Fig. 1), this jet actually exhibits an undulatory structure on any daily weather chart over the region between North Africa and the tropical North Atlantic. The application of the Lorenz energetics scheme to illustrate the AEW–AEJ interaction may face some difficulties: 1) because length scales of AEW and the AEJ are regional, it may be difficult to meaningfully separate the summer atmospheric circulation of North Africa into zonal-mean and eddy components required by this energetics scheme (Lorenz 1967); 2) because the Lorenz energy cycle was developed for a closed domain, its application to an open system is delicate in selecting the system's lateral boundary and the energy conversion from more than one possible expression (Wiin-Nielsen and Chen 1993). To avoid these uncertainties in dealing with the AEW–AEJ interaction with the Lorenz energy cycle, we need 1) a feasible scheme of separating the AEJ and AEW components of any field variable, and 2) a proper diagnostic scheme to illustrate this interaction.

a. AEW–AEJ spatial relationship

1) SEPARATION SCHEME

The maximum east–west extent of the AEJ (from North Africa to the North Atlantic) is about 120° in longitude, while the AEW wavelength is roughly 2000–4000 km. Length scales of the AEJ and AEW are equivalent wavenumbers 3 and 9–18, respectively, at 15°N. To explore the AEW–AEJ relationship/interaction, a spatial Fourier separation is used to divide any variable into its long (wavenumbers 0–5) and short (wavenumbers 6–31) wave regimes. For convenience, variables in these two wave regimes are designated by $()^L$ and $()^S$, respectively. The most unstable modes of the AEJ are wavenumber 11 by Simmons (1977) and wavenumbers 10–11 by Thorncroft and Hoskins (1994a). The scale separation introduced here to isolate AEWs agrees well with the growth rate of the AEJ unstable modes estimated by these studies.

Let us use an AEW_n (13 July 1979) and an AEW_s (30 August 1979) to test the feasibility of this separation scheme. Shown in Fig. 11 are the total zonal wind u and streamfunction ψ at 600 mb (top row), and their long-

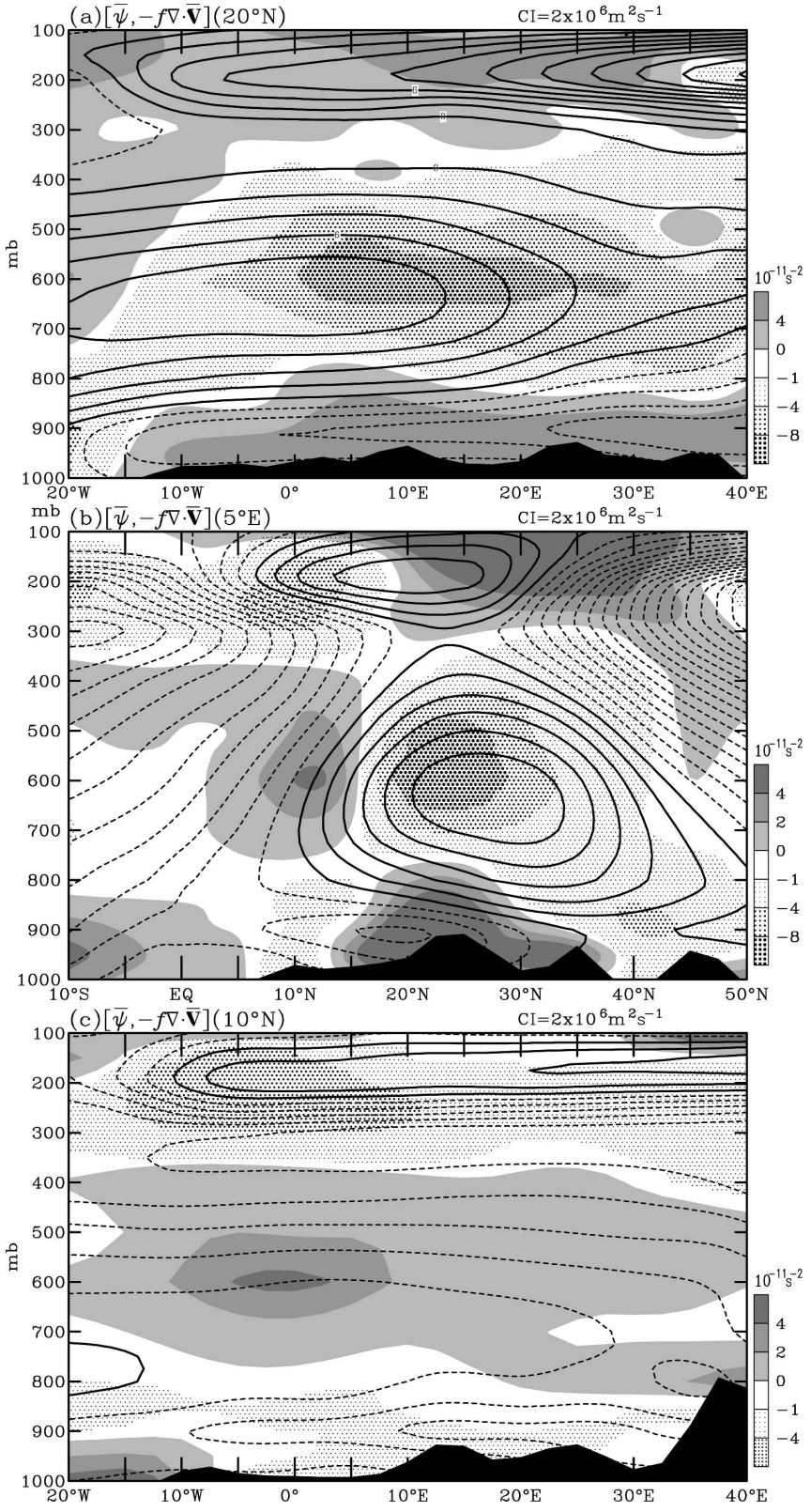

FIG. 9. Same as in Fig. 8 but for vortex stretching ($-f\nabla\cdot\overline{\mathbf{V}}$) superimposed on $\overline{\psi}$. The contour interval of the former variable is shown by the scale shown in the bottom-right-hand corner of (a) and (b).

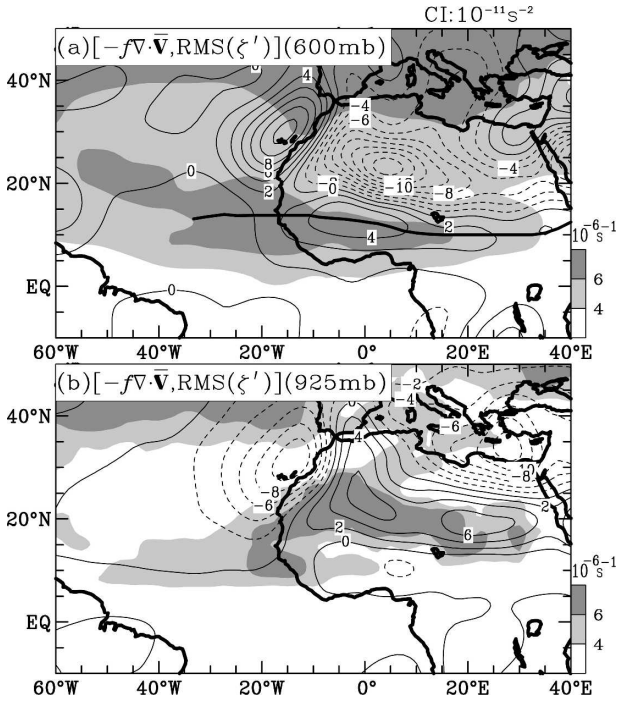

FIG. 10. The 1991–2000 summer-mean (JJAS) RMS values of the 2–7-day filtered vorticity ζ' superimposed on vortex stretching ($-f\nabla\cdot\bar{\mathbf{V}}$) at (a) 600 and (b) 925 mb. The AEJ core is indicated by a thick, solid line in (a). The contour interval of $-f\nabla\cdot\bar{\mathbf{V}}$ is shown at the right top of (a), while that of RMS(ζ') is shown by the scale in the bottom-right-hand corner of both (a) and (b).

and short-wave components of the two selected AEW cases: $(u, \psi)^L$(600 mb) (middle row) and $(u, \psi)^S$(600 mb) (bottom row), respectively. The ridge (thick dashed) and trough (thick solid) lines of both AEWs are superimposed; troughs of short-wave trains are juxtaposed with ridges on their east and west sides. Negative (positive) values of u^S(600 mb) appear in the northern (southern) part of negative (cyclonic) ψ^S(600 mb) cell. In contrast, the structure of u^S(600 mb) values associated with a positive (anticyclonic) ψ^S(600 mb) cell is opposite to that of a negative ψ^S(600 mb) cell. An east–west elongated strip of u^L(600 mb) ≤ -5 m s^{-1} (stippled areas in the middle row of Fig. 11) forms the basic structure of the AEJ along the southern rim of the Saharan high depicted by ψ^L(600 mb). Because total zonal wind u(600 mb) is a combination of u^L(600 mb) and u^S(600 mb), the undulatory structure of total wind speed u(600 mb) (top row in Fig. 11) is primarily established by u^S(600 mb) of the AEW$_n$/AEW$_s$ short-wave train. The surface low centers of the two selected AEW cases are marked by crosses; the AEW$_n$ surface low center is located north of the AEJ, while the AEW$_s$ is situated south of the AEJ. Based on a linear combination of u^L(600 mb) and u^S(600 mb), the zonal wind speed becomes higher when the AEJ and the AEW$_s$ trough and/or AEW$_n$ ridge are collocated, but becomes lower when the AEJ and the AEW$_s$ ridge/AEW$_n$ trough are superimposed. This kinematic relationship between AEW$_n$ and/or AEW$_s$ and the AEJ appears in all identified AEWs.

2) FURTHER SPATIAL RELATIONSHIP

Because the AEJ is part of the Saharan high (Fig. 11), variations in the AEJ may not only be caused by the AEW–AEJ interaction, but also by the Saharan high. An indication of this possibility may be revealed from a latitude–time diagram of u^L(600 mb, 5°W). To serve this purpose, summer 1979 is selected as a typical example to show the daily *maximum* easterly of u^L (i.e., the AEJ at 5°W), connected by a thick dashed line in Fig. 12a. The intensity variation of the AEJ is more discernable with the kinetic energy departure $\Delta KE_u^L \equiv \Delta\{1/2[u^L(600 \text{ mb}, 5°W)]^2\}$ (thick solid line in Fig. 12b). This kinetic energy departure is computed by the following procedure. First, KE_u^L $\{=1/2[u^L(600 \text{ mb}, 5°W)]^2\}$ and $KE_{\bar{u}}^L$ $\{=1/2[\bar{u}^L(600 \text{ mb}, 5°W)]^2\}$ were computed at every 2.5° grid over a 5° latitude zone centered at the latitude of daily maximum u^L(600 mb, 5°W) shown in Fig. 12a. Note that $\bar{u}$(600 mb, 5°W) is the seasonal-(JJAS) mean value of daily maximum u(600 mb, 5°W). Here ΔKE_u^L $(=KE_u^L - KE_{\bar{u}}^L)$ was then computed and averaged over the 5° latitude zone. On the other hand, the kinetic energy departure computed with u(600 mb, 5°W) including contributions from AEW$_n$ and/or AEW$_s$ is estimated by $\Delta KE_u \equiv \Delta\{1/2[u(600 \text{ mb}, 5°W)]\}$ (not shown to avoid any visible complication of the relationship between AEWs and the AEJ revealed from Fig. 12b). Let RMS represent the root-mean-square value. The ratio of RMS($\Delta KE_u - \Delta KE_u^L$)/RMS($\Delta KE_u^L$) is about 10%. Obviously, the primary contribution to the intensity variation of the AEJ comes from u^L. What is the synoptic or dynamic implication of the u^L contribution to the AEJ intensity variation?

Passages of the AEW$_n$ and AEW$_s$ troughs across 5°W are marked by "N" and "S," respectively, on the time series of ΔKE_u^L(600 mb, 5°W). As shown in Fig. 11, passage of the AEW$_n$ (AEW$_s$) ridge may be accompanied by an increase (decrease) of ΔKE_u^L(600 mb, 5°W). For such a synoptic condition, the N_H (S_H) symbol is added on the ΔKE_u^L(600 mb, 5°W) time series. An unexpected interesting feature of the ΔKE_u^L(600 mb, 5°W) temporal variation emerges: ΔKE_u^L(600 mb, 5°W) maximum >0 during most passages of AEW$_s$ troughs across 5°W and ΔKE_u^L(600 mb, 5°W) minimum <0 during most passages of AEW$_n$ troughs across 5°W. Previous studies of the AEW energetics have shown that energy

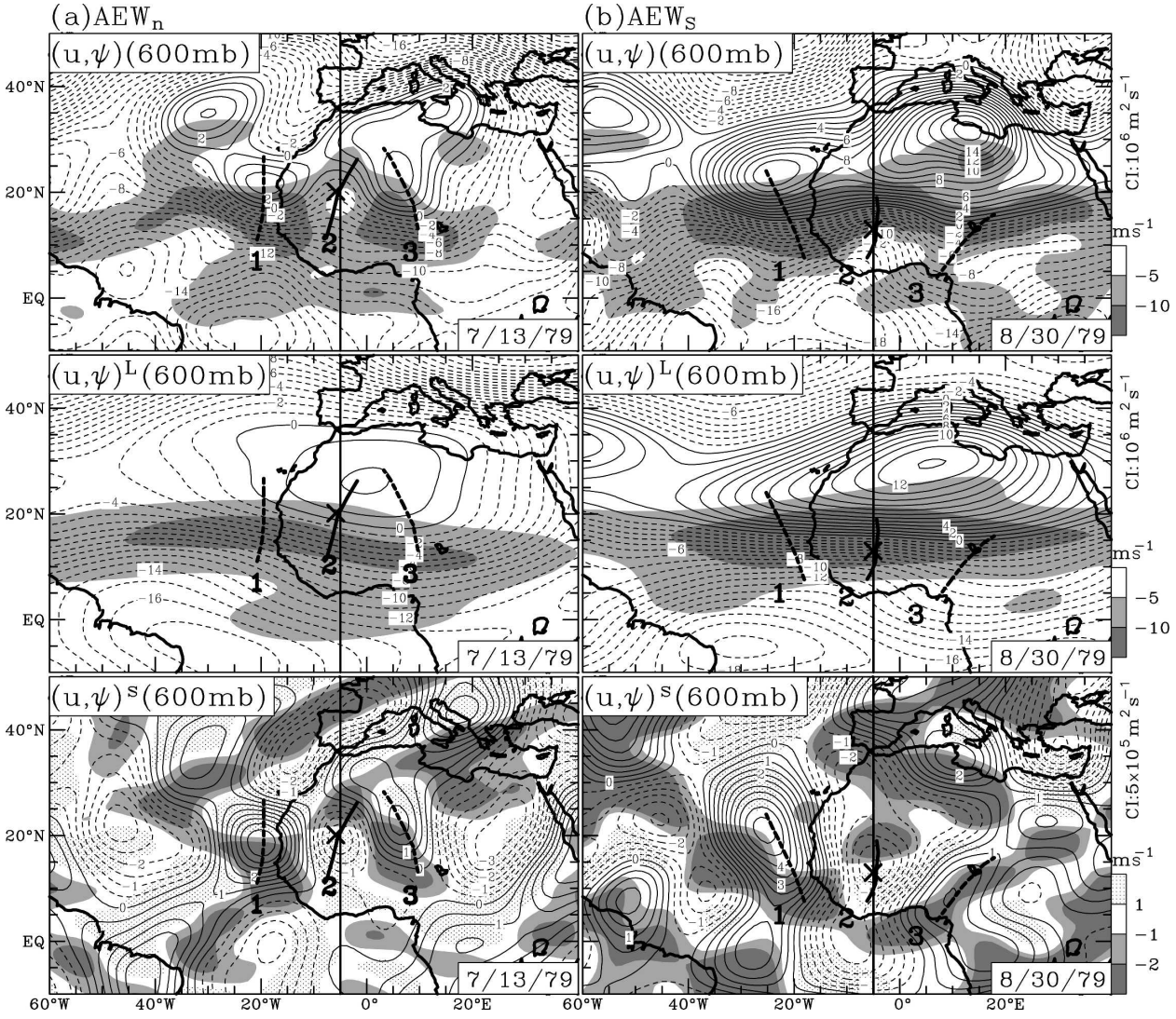

FIG. 11. The separation of the (top) (u, ψ)(600 mb) fields of (left) an AEW_n case and (right) an AEW_s case into the long-wave regime, (middle) $(u, \psi)^L$(600 mb), and (bottom) the short-wave regime $(u, \psi)^S$(600 mb). Contour intervals of ψ(600 mb), ψ^L(600 mb), and ψ^S(600 mb) are 10^6 m^2 s^{-1}, 10^6 m^2 s^{-1}, and 5×10^5 m^2 s^{-1}, respectively. For zonal winds, only easterlies of u and u^L are presented by stippled areas, but both easterlies and westerlies of u^S are displayed by stippled and dotted areas, respectively. Scales of u, u^L, and u^S are shown in the bottom-right-hand side of each panel in (a).

is extracted out of the AEJ to maintain these waves through the barotropic energy conversion west of the African continent. One may expect the decrease of ΔKE_u^L(600 mb, 5°W), that is, the decrease of the AEJ intensity, by its interaction with AEW through barotropic energy conversion. The temporal variation of ΔKE_u^L(600 mb, 5°W) and passages of AEW_n and/or AEW_s (Fig. 12b) reveal a dynamic relationship between the AEJ and AEWs different from that reflected by the conventional AEW energetics analysis.

The AEJ is part of the Saharan high. What is the role played by this midtropospheric anticyclone in the relationship between AEWs and the AEJ? Let us compare the $(u, \psi)^L$(600 mb) fields (Fig. 11) between 30 August 1979 [passage of an AEW_s trough and a ΔKE_u^L (600 mb, 5°W) maximum] and 13 July 1979 [passage of an AEW_n trough and a ΔKE_u^L(600 mb, 5°W) minimum]. The ψ^L(600 mb) maximum of the former case (middle panel in Fig. 11b) is larger than that of the latter case (middle panel in Fig. 11a). In other words, the Saharan high is stronger in the former than the latter. This comparison indicates that *the intensification/weakening of the AEJ and the Saharan high occurs simultaneously*. However, this observation is only based on two AEW cases. To support this observation, the relationship between the AEJ and the Saharan high was examined for all iden-

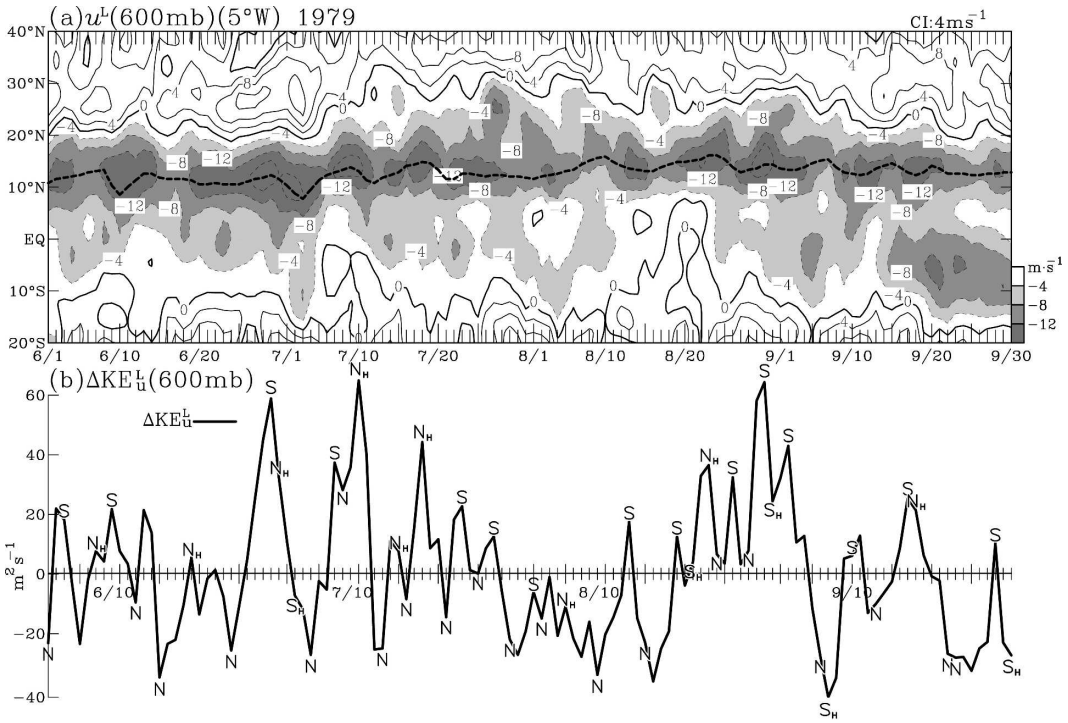

FIG. 12. (a) The summer 1979 latitude–time diagram of u^L(600 mb) at 5°W superimposed with a thick, dashed line connecting maximum easterlies of u^L(600 mb), and (b) time series of ΔKE^L_u(600 mb) (thick, solid line). The ΔKE^L_u is departure of KE^L_u from its corresponding summer-mean (JJAS) value. Here N and S are marked, respectively, on the ΔKE^L_u time series during passages of the AEW_n and AEW_s troughs across 5°W. Passages of the AEW_n and AEW_s ridges resulting in noticeable ΔKE^L_u(600 mb, 5°W) are denoted by N_H and S_H, respectively.

tified AEWs. The intensity of the Saharan high is defined by a 5° latitude × 5° longitude area-mean $\Delta\psi^L$(600 mb) [$\equiv\psi^L$(600 mb $-$ $\overline{\psi}^L$(600 mb); where the overbar $\equiv$ summer-mean value] around the maximum or minimum value of ψ^L(600 mb) at 5°W within the North African continent. The scatter diagram of ΔKE^L_u(600 mb, 5°W) versus $\Delta\psi^L$(600 mb) for all identified AEWs is shown in Fig. 13. AEW_ns are denoted by open circles and AEW_ss by dots. If the relationship between intensities of the AEJ and the Saharan high follows our observation in Fig. 11, we expect that AEW_ns are clustered over the quadrant [ΔKE^L_u(600 mb, 5°W) < 0, $\Delta\psi$(600 mb) < 0] and AEW_ss over the quadrant [ΔKE^L_u(600 mb, 5°W) > 0, $\Delta\psi$(600 mb) > 0]. This expectation is confirmed by the scatter diagram of ΔKE^L_u versus $\Delta\psi$ in Fig. 13: a close correlation exists between intensities of the AEJ and the Saharan high. More importantly, intensities of both elements of the North African summer circulation function as a separator of the westward-propagating AEW_ns and AEW_ss across 5°W: *Most AEW_ns (AEW_ss) troughs propagate across West Africa when the AEJ and the Saharan high are weak (strong).*

A coherent relationship between AEWs along the two propagation paths was suggested by previous studies (e.g., Pytharoulis and Thorncroft 1999; Fink et al. 2004). The population contrast between AEW_n and AEW_s (Fig. 7) and the separated westward propagations of these two types of AEWs determined by the AEJ intensity do not seem to support the coherent westward propagation scenario between AEW_n and AEW_s. In view of this argument, the relationship and interaction of the AEJ with most AEW_n and AEW_s should be independent. The westward propagations of AEW_n and AEW_s are clearly revealed from the 1979 *x–t* diagrams of ψ^s_n(600 mb, 20°N) and ψ^s_s(600 mb, 10°N) in Figs. 14a,c, respectively. Longitudinal locations of both AEW_n (indicated by N) and AEW_s (indicated by S) on the *x–t* diagram of u^L(600 mb, 15°N) (Fig. 14b) show that most AEW_s tracks follow strong easterlies, while the majority of AEW_n tracks coincide with weak easterlies. Although these two types of AEWs propagate with about the same speed, only 6 out of 20 AEW_ns and 15 AEW_ss propagate coherently westward. No obvious coherent relationship exists between them. Following Fig. 14b, the *x–t* diagrams of u^L(600 mb) at 15°N superimposed with longitudinal locations of AEWs for 1991–2000 were examined.

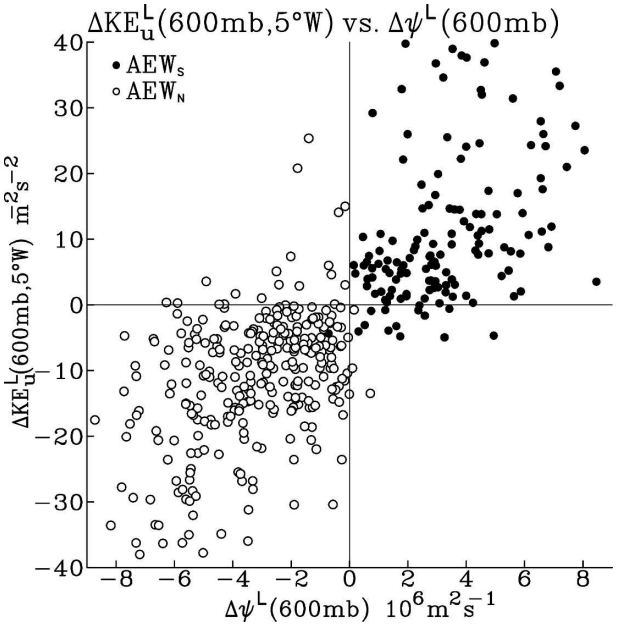

FIG. 13. Scatter diagram of ΔKE_u^L(600 mb, 5°W) vs $\Delta\psi^L$(600 mb) for trough crossings of both AEW_ns (open circles) and AEW_ss (dots) at 5°W. The $\Delta\psi^L$(600 mb) is an area-mean value of ψ(600 mb) − $\bar{\psi}$(600 mb) over a 5° lat × 5° lon box around the maximum or minimum value of this difference at 5°W. Here $\bar{\psi}$(600 mb) is the 1991–2000 summer-mean ψ(600 mb) field.

Populations of AEW_n, AEW_s, correlated cases, and combined AEW_n and AEW_s for every summer over this 10-yr period are shown in Fig. 15. As in the 1979 summer case, correlated AEW_ns and AEW_ss represent only a small population of AEWs.

b. AEW–AEJ interaction

It was revealed from Fig. 13 that the temporal variation of the AEJ mainly follows that of the Saharan high. On the other hand, the *x–t* diagram of u^L(600 mb) at 15°N superimposed with longitudinal locations of AEWs in Fig. 14b indicates strong (weak) u^L(600 mb, 15°N) is coupled with the westward propagation of AEW_ss (AEW_ns). In other words, this relationship persistently exists between the AEJ and the two types of AEWs. Therefore, constant zonal wind speeds of the AEJ were often assumed by numerical simulations of AEW genesis and development with simplified global models (e.g., Thorncroft and Hoskins 1994a,b). Implying an unlimited energy supply by the AEJ and no energy feedback from AEWs to the AEJ, this assumption is consistent with the negligible feedback from AEWs to the AEJ reflected by Figs. 13 and 14b. Therefore, we shall focus the AEW–AEJ interaction on the impact of the AEJ on the evolution of AEWs.

Because AEWs are well portrayed by ψ^S, AEW evolution/development can be illustrated by its tendency, ψ_t^S ($\equiv\partial\psi^S/\partial t$). Despite numerous applications of the Lorenz energetics scheme to explore the AEW–AEJ interaction, some uncertainties of this approach were pointed out earlier. In addition, it is difficult to illustrate synoptically the AEW–AEJ interaction through energy conversions. On the contrary, Sanders's (1984) application of the streamfunction tendency to examine the development of monsoon depressions suggests an alternative way to synoptically explore the ψ^S tendency caused by different dynamical processes through the inverse Laplace transform of the vorticity equation. Following Sanders (1984), we may write the ψ^S equation as

$$\underbrace{\left[\nabla^{-2}\left(\frac{\partial\zeta}{\partial t}\right)\right]^S}_{\psi_t^S} = \underbrace{\{\nabla^{-2}[-\mathbf{V}\cdot\boldsymbol{\nabla}(\zeta+f)]\}^S}_{\psi_A^S} + \underbrace{[\nabla^{-2}(\zeta+f)\boldsymbol{\nabla}\cdot\mathbf{V}]^S}_{\psi_\chi^S}. \quad (2)$$

The notation used in Eq. (2) is conventional: ζ, f, and $\mathbf{V}$ are relative vorticity, Coriolis parameter, and velocity vector, respectively. In Eq. (2), tendency ψ_A^S may be expressed as

$$\psi_A^S = \underbrace{[\nabla^{-2}(-\mathbf{V}\cdot\boldsymbol{\nabla}\zeta)]^S}_{\psi_{A1}^S} + \underbrace{[\nabla^{-2}(-v\beta)]^S}_{\psi_{A2}^S}. \quad (3)$$

For AEWs, relative vorticity advection is generally much larger in magnitude than the meridional advection of planetary vorticity, and so ψ_{A1}^S is much larger than ψ_{A2}^S. It was shown in Fig. 11 that the zonal wind component contributed by the AEJ is much larger than that by AEWs, that is, $|u^L| \gg |u^S|$. Therefore, one may expect the following approximation:

$$\psi_{A1}^S \simeq [\nabla^{-2}(-\mathbf{V}^L\cdot\boldsymbol{\nabla}\zeta)]^S \equiv \psi_{A1L}^S.$$

The impact of the AEJ on the evolution of AEWs may be achieved through ψ_{A1}^S. The application of the ψ^S budget to the AEW–AEJ interaction is illustrated by the two cases of AEWs crossing 5°W presented in Fig. 11: the AEW_n on 13 July 1979 and the AEW_s on 30 August 1979.

1) AEW_N CASE (13 JULY 1979)

A minimum ΔKE_u^L appears on 13 July 1979 (Fig. 12b). At this time, a short-wave train, shown in the

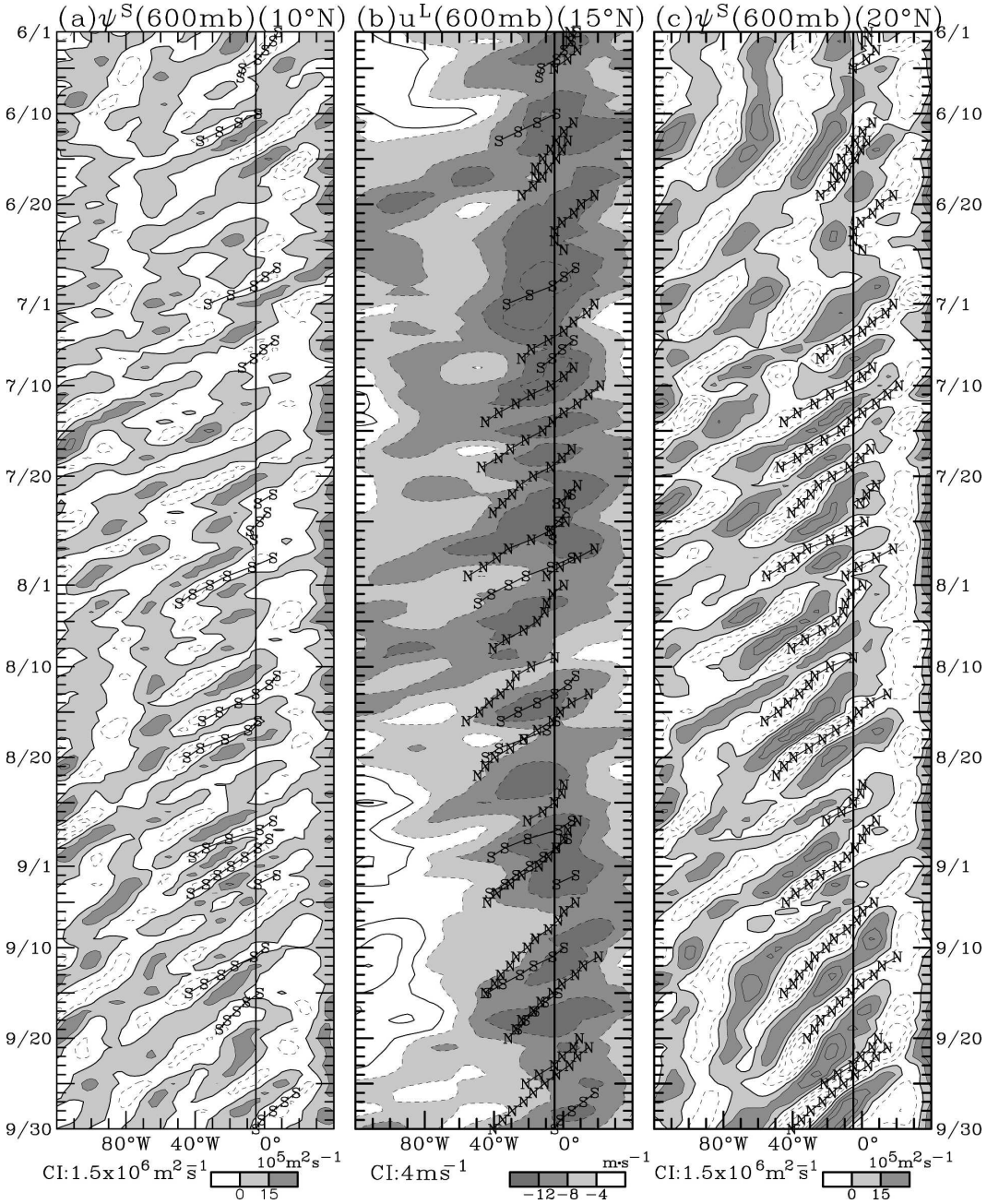

FIG. 14. The x–t diagrams of (a) ψ^S(10°N), (b) u^L(15°N), and (c) ψ^S(20°N) at 600 mb during summer 1979. Longitudinal locations of AEW_s and AEW_n are marked by S and N, respectively, on the x–t diagrams. The location of 5°W is denoted by a thick, solid line. Contour intervals of all three variables are shown at the bottom left of (a)–(c). To make these diagrams more readable, all three variables are shaded by the scale shown at the bottom right of (a)–(c).

600-mb streamline chart (Fig. 16a), is located north of the AEJ along the southern periphery of the Saharan high. This AEW_n wave train consists of a trough (marked "2") juxtaposed with a ridge to its west (marked 1) and another ridge to its east (marked "3"). As illustrated by Fig. 11, easterlies are strengthened by the two AEW_n ridges, but weakened by the AEW_n troughs. According to Eq. (2), ψ_t^S is a result of the combined dynamical processes in the rhs of this equation. Various terms of the ψ^S(600 mb) budget during passage of trough 2 are displayed in Figs. 16a–e: positive (negative) streamfunction tendencies are denoted by dotted (stippled) areas. Salient features of this budget are highlighted as follows:

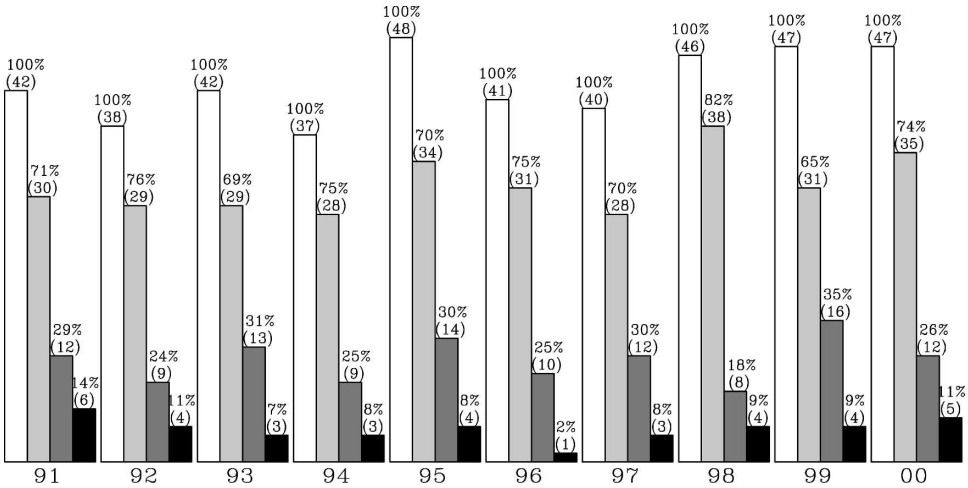

FIG. 15. Population histograms of AEW (open histogram), AEW_n (gray histogram), AEW_s (dark histogram), and coherent westward-propagating AEW_n/AEW_s (black histogram) for each year from 1991 to 2000. The population percentage of each group is shown on the top of its population histogram.

1) In Fig. 16b, ψ_t^S(600mb) (dotted/stippled area) exhibits positive (negative) anomalies west of the positive (negative) ψ^S(600 mb) cell (contour) representing ridge 1 (trough 2) of the AEW_n. This ψ_t^S–ψ^S spatial quadrature relationship results in the westward propagation of this AEW_n.
2) The contrast between ψ_χ^S(600 mb) (Fig. 16c) and ψ_A^S(600 mb) (Fig. 16d) shows that the ψ^S tendency generated by vortex stretching plays a minor role in developing/maintaining the AEW_n wave train at this stage compared with the ψ^S tendency generated by vorticity advection, namely ψ_t^S(600 mb) $\approx$ ψ_A^S(600 mb).
3) Although the meridional advection of planetary vorticity ($-v\beta$) (not shown) is not completely negligible, the ψ_A^S(600 mb) tendency is dominated by relative vorticity advection ($-\mathbf{V}\cdot\nabla\zeta$). The AEJ was well depicted by u^L(600 mb) in Fig. 11. The effect of the AEJ on the AEW_n evolution can be realized by the similar spatial structure and comparable magnitude between ψ_A^S(600 mb) (Fig. 17d) and ψ_{A1L}^S(600 mb) (Fig. 17e) along the AEW_n wave train.

Because $-\mathbf{V}^L\cdot\nabla\zeta$ plays a major role in propagating and developing the AEW_n wave train, the impact of the AEJ on the AEW_n activity is primarily accomplished by relative vorticity advection.

2) AEW_s CASE (30 AUGUST 1979)

A maximum ΔKE_u^L appeared on 30 August 1979. As shown in Fig. 11, the spatial relationship between the AEJ and the AEW_s short-wave train (Fig. 16f) is opposite to that between the AEJ and the AEW_n short-wave train (Fig. 16a). The ridge of AEW_s weakens the AEJ, while the trough of AEW_s intensifies this jet. The ψ^S(600 mb) anomalies representing the AEW_s short-wave train are spatially in quadrature with ψ_t^S(600 mb) anomalies (Fig. 16g); negative (positive) ψ_t^S anomalies are ahead (i.e., west) of negative (positive) ψ^S(600 mb) anomalies. This ψ_t^S–ψ^S spatial relationship, which is a result of the imbalance between ψ_A^S(600 mb) (Fig. 16i) and ψ_χ^S(600 mb) (Fig. 16h), enables the AEW_s wave train to propagate westward. The resemblance between ψ_A^S(600 mb) and ψ_{A1L}^S(600 mb) (Fig. 16j) indicates that relative vorticity advection by the AEJ is also the major dynamic process in developing AEW_s. Regardless of the difference in their genesis mechanisms, the ψ^S(600

→

FIG. 16. (a) The 600-mb streamline chart when ΔKE_u^L(600 mb, 5°W) reaches its minimum value on 13 Jul 1979 during the passage of an AEW_n across 5°W embedded in a short-wave train (its ridge–trough–ridge structure marked by 1–2–3), and (b)–(e) three terms of the ψ^S(600 mb) budget and ψ_{A1L}^S(600 mb) superimposed on ψ^S(600 mb) (contours). On 30 Aug 1979, ΔKE_u^L(600 mb, 5°W) reaches its maximum value during the passage of an AEW_s across 5°W. (f)–(j) The 600-mb streamline chart and the ψ^S(600 mb) budget and ψ_{A1L}^S(600 mb) corresponding to those of the 13 Jul 1979 AEW_n case. The surface low center coupled with the 600-mb trough of either AEW_n or AEW_s is marked by a cross. The trough and ridge lines of AEWs are denoted by thick, solid and thick, dashed lines, respectively. The contour interval of ψ^S(600 mb) is 5×10^5 m^2 s^{-1}, while scales of various streamfunction tendencies are shown in the bottom-right-hand side of (h)–(j). Scale of 600-mb isotach is displayed in the bottom-right-hand side of (f)–(j).

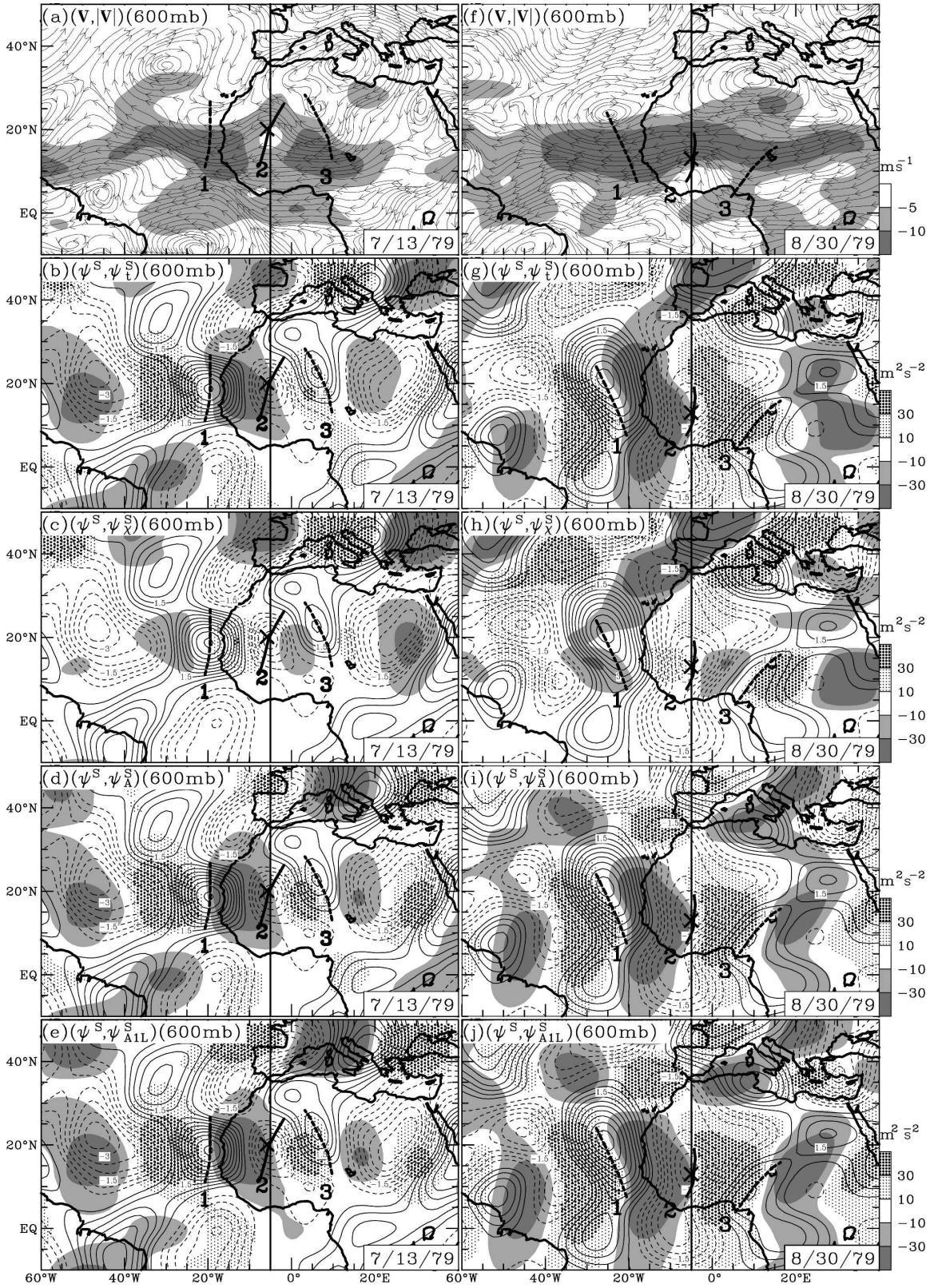
(a)(V,|V|)(600mb)
(f)(V,|V|)(600mb)
(b)(ψ^S,ψ^S_t)(600mb)
(g)(ψ^S,ψ^S_t)(600mb)
(c)(ψ^S,ψ^S_χ)(600mb)
(h)(ψ^S,ψ^S_χ)(600mb)
(d)(ψ^S,ψ^S_A)(600mb)
(i)(ψ^S,ψ^S_A)(600mb)
(e)(ψ^S,ψ^S_A1L)(600mb)
(j)(ψ^S,ψ^S_A1L)(600mb)
7/13/79
8/30/79
40°N
20°N
EQ
60°W
40°W
20°W
0°
20°E
ms^-1
m^2s^-2
30
10
−10
−30
−5
1
2
3

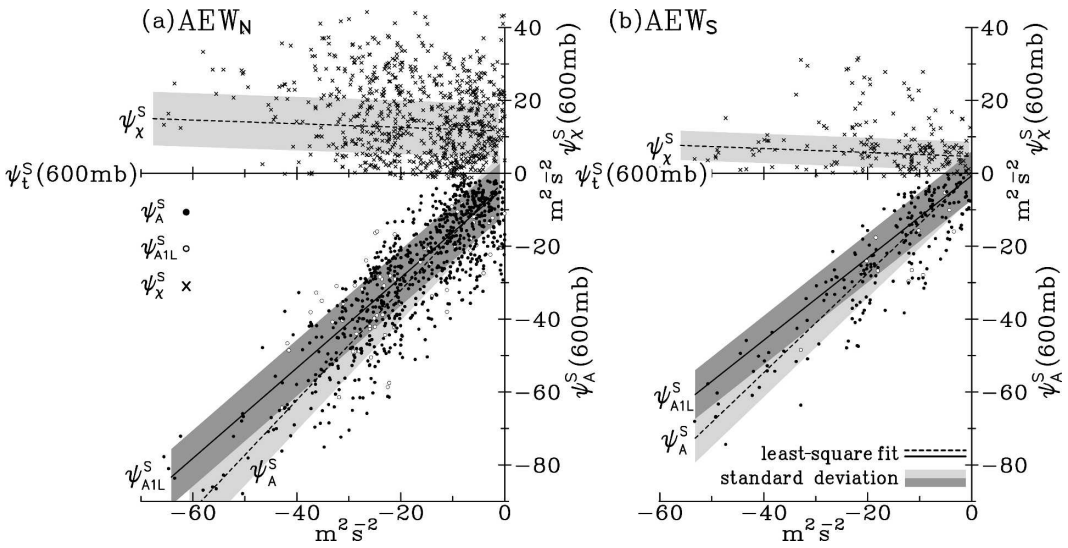

FIG. 17. Scatter diagrams of ψ_t^S(600 mb) vs [ψ_A^S(600 mb), ψ_{A1L}^S(600 mb)] and ψ_t^S vs ψ_χ^S(600 mb) over a 2.5° × 2.5° box encircling the minimum (maximum) centers of ψ_A^S(600 mb), ψ_{A1L}^S(600 mb), and ψ_χ^S(600 mb): scatters of these three variables are marked by dots, open circles, and crosses, respectively. Standard deviation (stippled area) and the least squares fit lines are also added on scatter diagrams.

mb) budget of AEW$_s$ shown in Figs. 16f–j behaves in the same way as that in the ψ_n^S(600 mb) budget of AEW$_n$ (Figs. 16b–e).

The analysis of the AEW–AEJ interaction through the streamfunction budget in the short-wave regime was performed only for two AEW cases (one AEW$_n$ and one AEW$_s$). Can the findings obtained from these two cases be applied to all identified AEW cases? Scatter diagrams of ψ_t^S(600 mb) versus [ψ_A^S(600 mb), ψ_{A1L}^S(600 mb)] and ψ_t^S(600 mb) versus ψ_χ^S(600 mb) for maximum values of these ψ^S tendencies west of centers of all negative ψ^S(600 mb) cells (representing all AEW$_n$ and AEW$_s$ troughs) across 5°W are shown in Fig. 17. The statistical mean values and departures of scatters in this figure are presented by the least squares fit (dashed) lines and standard deviations (stippled areas) from these mean values. Scatters of ψ_t^S versus ψ_χ^S are nearly distributed along a least squares fit line almost parallel to the $\psi_t^S = 0$ axis. As indicated by these scatter diagrams, ψ_χ^S is always positive, but small, regardless of the ψ_t^S magnitude. All scatters of ψ_t^S versus (ψ_A^S, ψ_{A1L}^S) are distributed along the least squares fit lines with a slope of almost 45° which indicates not only magnitudes of ψ_A^S and ψ_{A1L}^S are comparable, but those of ψ_t^S and (ψ_A^S, ψ_{A1L}^S) of all identified AEWs are also comparable. The conclusion drawn from these scatter diagrams is that the westward propagation of AEWs across 5°W and the evolution of these waves are primarily determined by their interaction with the AEJ through vorticity advection by this jet.

6. Concluding remarks

The AEW characteristics presented by previous studies may be summarized by the following four major features: two propagation paths (one north of the AEJ and another south of the AEJ), two possible genesis mechanisms (the barotropic–baroclinic instability south of the AEJ and the baroclinic instability of a shallow low-static stability layer north of the AEJ), vertical development of AEWs (AEW$_n$ confined in the lower troposphere near the surface and AEW$_s$ in the midtroposphere), and a strong interaction between the AEJ and AEWs. These features lead to the following concerns of AEW activity:

1) What is the population contrast of AEWs between the northern (AEW$_n$) and southern (AEW$_s$) propagation paths?
2) How does the low-level circulation of North Africa affect the C–T baroclinic instability mechanism of AEW$_n$? Can this mechanism be more effective than the barotropic–baroclinic instability mechanism in generating AEW$_s$?
3) Why are the vertical developments of AEW$_n$ and AEW$_s$ restricted to different layers of the troposphere?
4) Can the AEW–AEJ interaction be illustrated in terms of the synoptic relationship between them?

The ERA-40 reanalyses for the 1991–2000 period supplemented with 1979 were analyzed to answer these questions because these reanalysis data were initialized with surface observations (Kalnay and Cai 2003; Käll-

berg et al. 2004). Major findings of the present study are as follows:

1) Based on the genesis frequency of the AEWs propagating across 5°W, the AEW_n population is approximately 2.5 times of the AEW_s population. The majority of AEWs over West Africa and off the West African coast are contributed by AEW_n.
2) The AEW_n genesis by the C–T baroclinic instability is facilitated by the collaborative effect of weak static stability and the intrusion of the Harmattan. Therefore, the AEW_n genesis occurs more frequently over the three convergent centers and the southwestward extension of the Saharan thermal low. Because the near-surface temperature exhibits a pronounced diurnal variation, the AEW_n genesis undergoes the same variation with their maximum occurrence at 1800 UTC (when the near-surface static stability is weakest).
3) Strong upward motion appears along the Saharan thermal low and in the midtroposphere south of the AEJ. Therefore, positive vortex stretching developed by upward motion in these two regions forms a positive vorticity source of the environmental flow below the Saharan high and the western part of the Asian monsoon high. Consequently, these two regions not only facilitate the westward propagation of AEW_n and AEW_s over North Africa, but also form an environment conducive to the layer-restricted development of AEWs.
4) Both AEW_n and AEW_s develop into their mature phase when they propagate westward across 5°W. The passage of AEW_n (AEW_s) across this longitude occurs when the AEJ and the Saharan high are weak (strong). These two circulation elements of North Africa function as a separator of these two types of westward-propagating AEWs. Because of this separation, westward propagations of most AEW_ns and AEW_ss are relatively independent. The AEW–AEJ relationship does not suggest a noticeable AEW feedback to affect the variation of the AEJ intensity. Illustrated synoptically through the streamfunction budget in the short-wave (waves 6–31) regime, the AEW–AEJ interaction is primarily accomplished through relative vorticity advection by the AEJ.

Tracing the wave history of AEW_s with the ECMWF operational archives, Reed et al. (1988a) found significant discrepancies between forecasts and observations, particularly over the data-sparse region of North Africa. However, compared with spectral analysis of upper-air observations at two stations close to the west coast of North Africa (one on the northern propagation path and another on the southern one), Pytharoulis and Thorncroft (1999) showed that the Met Office global model analysis contains all major features of the AEW activity. We may not be able to claim that the ERA-40 reanalyses are free of data assimilation system bias, but all major basic features of the AEW activity observed by previous studies are well depicted by the ERA-40 reanalyses. It is certainly our hope that a denser network of upper-air observations will be developed over North Africa in such a way that the new findings of the present study can be further verified. Nevertheless, these findings are informative and helpful in our future search for AEW dynamics and the impact of AEW activity on North African climate change.

Approximately half of the North Atlantic tropical cyclones (TCs) and tropical storms (TSs) develop from AEWs. Thorncroft and Hodges (2001) argued that AEW_ns do not contribute to this transformation of AEWs into TC or TS. Despite the population ratio of AEW_n/AEW_s (~2.5), it was observed by the preliminary result of a companion study that the ratio of TC and TS developed from AEW_ns and AEW_ss is about 1.7. The contrast between these two ratios indicates that AEW_ns are less effective in transforming into TC or TS, but not completely negligible. In view of contributions to North Atlantic TC and TS formation from these two types of AEWs, new findings of AEW activity are useful in improving the formation forecasts of North Atlantic TC or TS. The AEJ and the Saharan high act as a separator of westward-propagating AEW_ns and AEW_ss. The impact of any climate change on the Atlantic TC/TS activity can be accomplished through the AEJ and the Saharan high. It has been observed that sub-Saharan rainfall has exhibited an interdecadal decline since 1960 (e.g., Nicholson et al. 2000). Because AEWs are an important rain producer of the sub-Saharan region, the location and intensity changes of the AEJ and the Saharan high may affect the population, propagation paths of AEW_n and AEW_s, and contributions of these two types of AEWs to the sub-Saharan rainfall decline in the past five decades. In short, the climatology of the AEW activity disclosed here paves the way for further study of the AEW characteristics and dynamics and the role played by AEWs in North African climate change.

Acknowledgments. This study, supported by the NSF Grant ATM0136220, was accomplished with computational assistance of Peter Hsieh, Paul Tsay, and Simon Wang. The final revision of this paper during the author's visit to National Central University (NCU) was partially supported by the NCU Development Program of Internationally Top-Ranked University sponsored by the Ministry of Education in Taiwan. Numerous

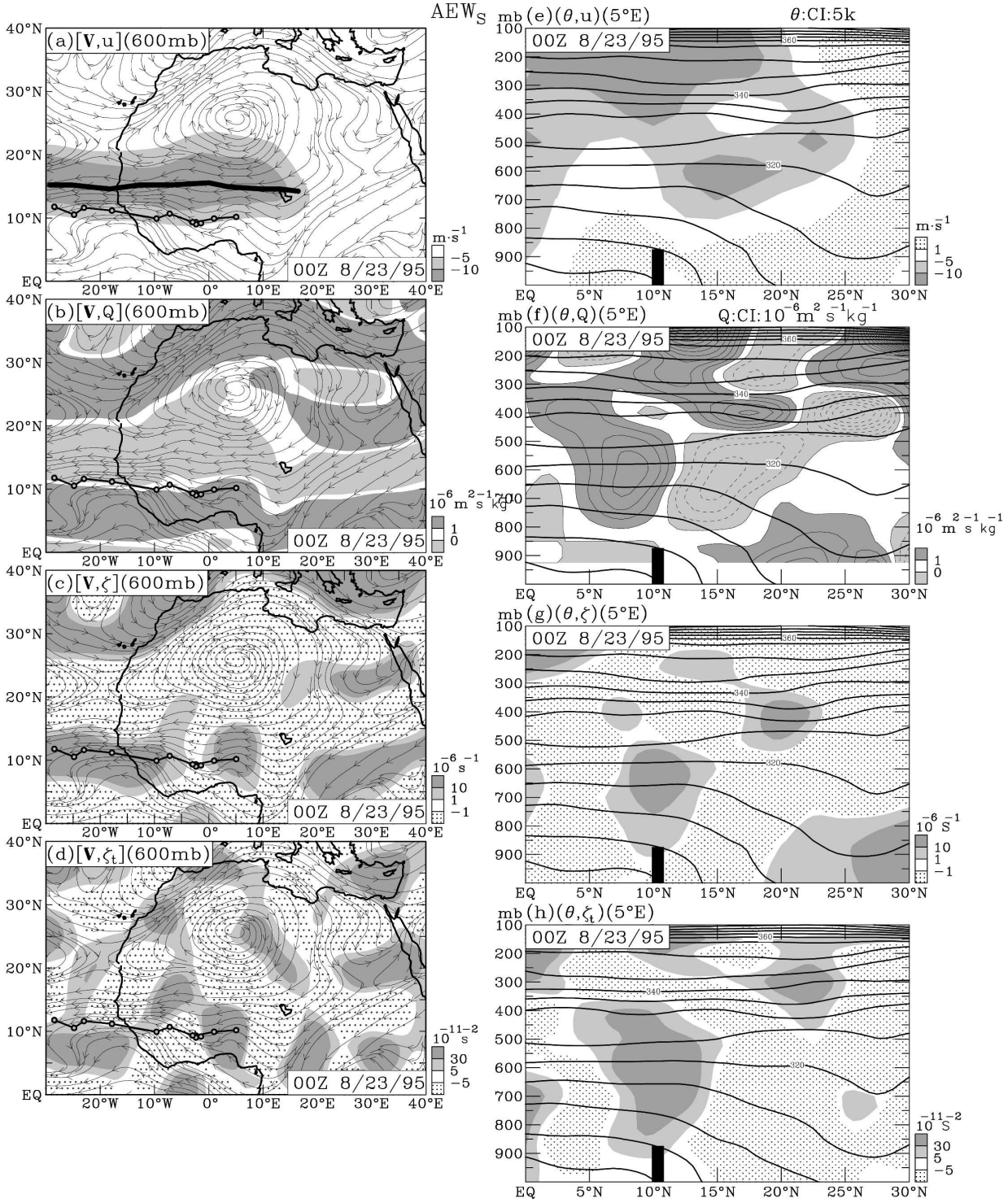

FIG. A1. The 600-mb streamline charts superimposed with (a) u(600 mb), (b) Q(600 mb), (c) ζ(600 mb), and (d) ζ_t(600 mb), and latitude–height cross sections of θ (thick, solid line) superimposed with (e) u, (f) Q, (g) ζ, and (h) ζ_t of an AEW$_s$ case at 0000 UTC 23 Aug 1995. The AEJ at 600 mb is marked by a solid line in (a). The longitudinal location of this AEW$_s$ is marked by a heavy black bar at the bottom of (e)–(h). Scales of u(600 mb) in (a), Q(600 mb) in (b), ζ(600 mb) in (c), ζ_t(600 mb) in (d), and their corresponding variables in the latitude–height cross sections (e)–(h) are located at the bottom-right-hand side of (a)–(h). The contour interval of θ for every cross section in the right column is 5 K, while that of Q in (f) is 10^{-6} m^2 s^{-1} K kg^{-1}.

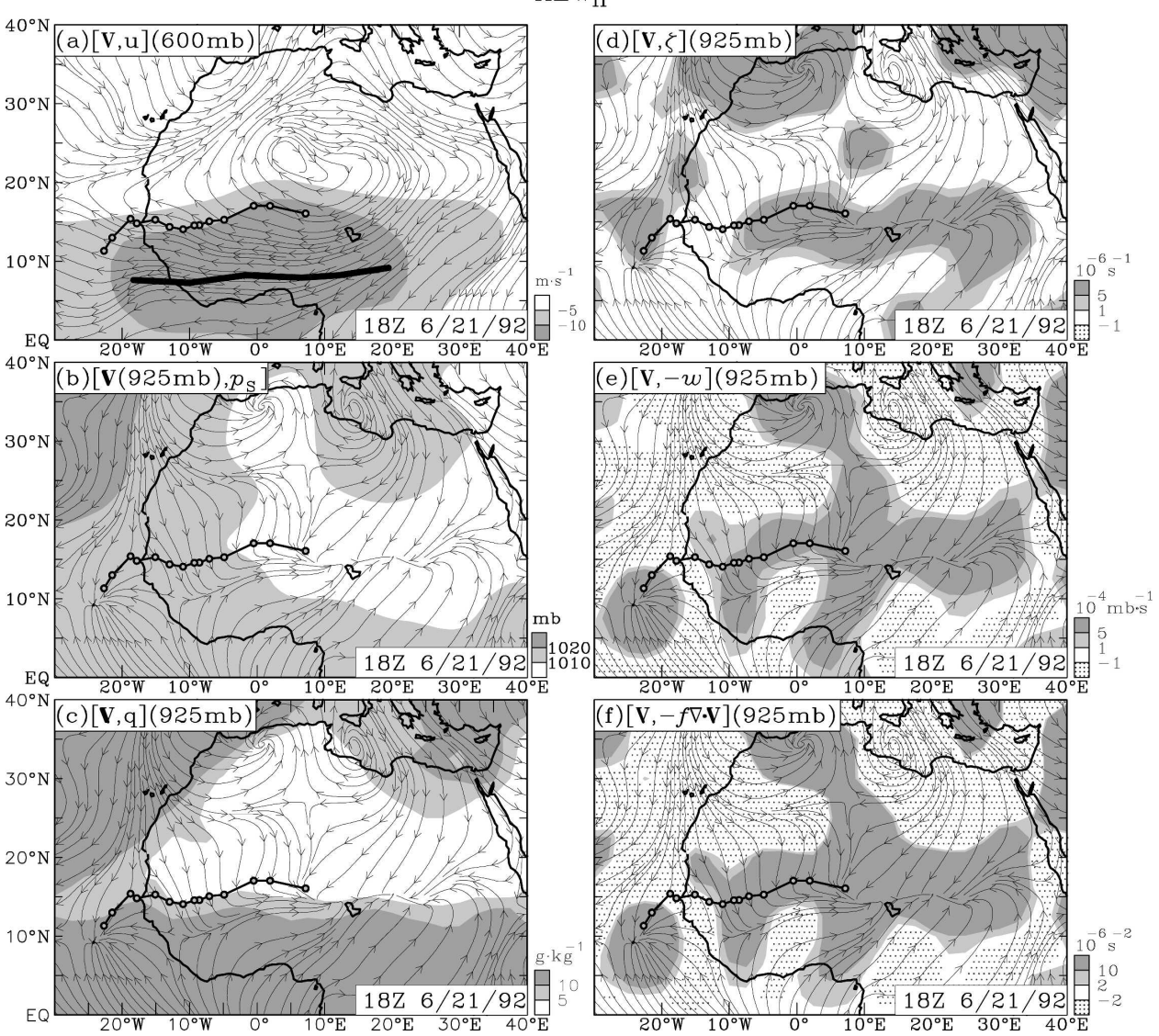

FIG. A2. The 600- or 925-mb streamline charts superimposed with (a) u(600 mb), (b) p_S, (c) q(925 mb), (d) ζ(925 mb), (e) $-\omega$(925 mb), and (f) $-f\nabla\cdot\mathbf{V}$(925 mb) of an AEW$_n$ case at 1800 UTC 21 Jun 1992. The AEJ at 600 mb is marked by a solid line. Scales of u(600 mb) in (a), p_S in (b), q(925 mb) in (c), ζ(925 mb) in (d), $-\omega$(925 mb) in (e), and $-f\nabla\cdot\mathbf{V}$(925 mb) in (f) are located at the bottom-right-hand side of (a)–(f).

comments offered by Dr. Fred Sanders and an anonymous reviewer were very helpful in improving this paper. Typing support and editing assistance provided by Judy Huang and Dave Flory, respectively, are highly appreciated.

APPENDIX

AEW Cases Used to Illustrate the Two Genesis Mechanisms

The two AEW genesis mechanisms outlined in section 3a are illustrated by the following two randomly selected AEWs in terms of streamline charts and latitude–height cross sections cutting through the perturbations at their genesis locations:

1) AEW$_s$ (at 0000 UTC 26 June 1992; Fig. A1): The maximum activity of AEW$_s$ is located at 600 mb (Fig. 2). The synoptic condition of the AEW$_s$ genesis is depicted by the 600-mb streamline charts superimposed with different variables in Figs. A1a–d and the latitude–height cross sections of θ superimposed with the corresponding variables in Figs. A1e–h. As indicated by the genesis location (i.e., the initial lo-

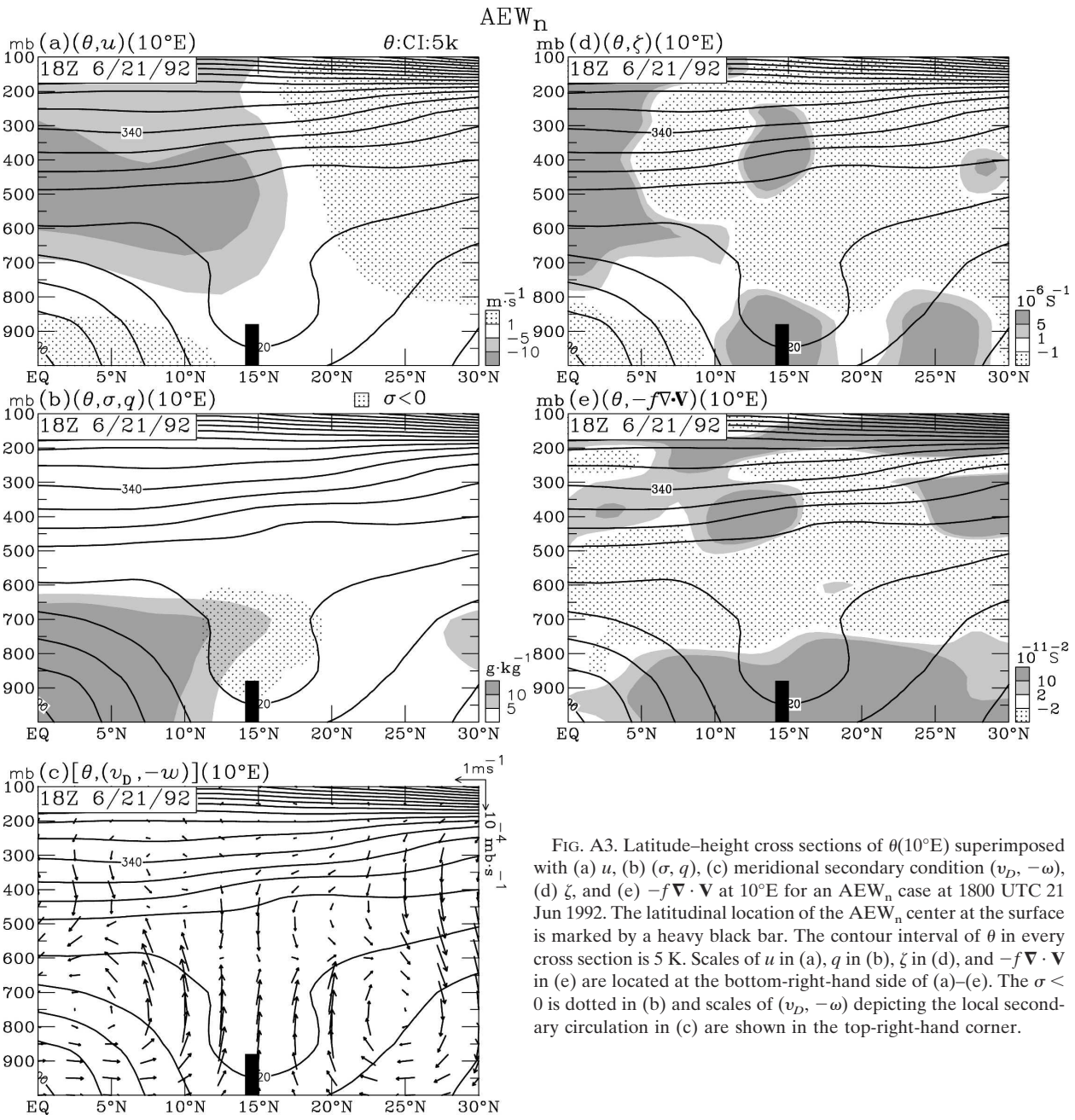

FIG. A3. Latitude–height cross sections of θ(10°E) superimposed with (a) u, (b) (σ, q), (c) meridional secondary condition (v_D, $-\omega$), (d) ζ, and (e) $-f\nabla\cdot\mathbf{V}$ at 10°E for an AEW$_n$ case at 1800 UTC 21 Jun 1992. The latitudinal location of the AEW$_n$ center at the surface is marked by a heavy black bar. The contour interval of θ in every cross section is 5 K. Scales of u in (a), q in (b), ζ in (d), and $-f\nabla\cdot\mathbf{V}$ in (e) are located at the bottom-right-hand side of (a)–(e). The $\sigma < 0$ is dotted in (b) and scales of (v_D, $-\omega$) depicting the local secondary circulation in (c) are shown in the top-right-hand corner.

cation of this AEW$_s$ path) and the ensuing propagation track (Fig. A1a), this AEW$_s$ is always located south of the AEJ (thick, solid line) along the southern rim of the Saharan anticyclone (Fig. A1a). Large-value positive vorticity ζ(600 mb) is associated with the identified AEW$_s$ perturbation (Figs. A1c,g). South of the AEJ, there are strong vertical and horizontal shears (Fig. A1e) where a sign change of Q_y appears in Figs. A1b,f. In addition to the sign change of Q_y, the negative Q_y gradient is coupled with the large positive θ_y gradient (Fig. A1f). The Charney–Stern criterion (Burpee 1972) is satisfied by the environmental flow of this AEW$_s$ and its development is supported by positive ζ_t(600 mb) (Figs. A1d,h).

2) AEW$_n$ (at 1800 UTC 21 June 1992; Figs. A2–A3): The genesis location (the initial location of this AEW$_n$ path) and propagation track of this AEW$_n$ are located north of the AEJ (Figs. A2a and A3a), but underneath the Saharan anticyclone (Fig. A2a).

This AEW_n genesis occurs along the surface convergence zone with $p_S < 1010$ mb (Fig. A2b) and north of the cool-moist monsoon air mass (Fig. A3b) along the line of $q \leq 5\text{g kg}^{-1}$ (Fig. A2c). Below 600 mb, static stability $\sigma \leq 0$, around the genesis location and $\theta_y > 0$ south of this location (Fig. A3b). The upward motion coupled with the surface convergence (Figs. A2e and A3e) facilitates the occurrence of the C–T instability. Consequently, positive vorticity ($\zeta > 0$ in Figs. A2d and A3d) is generated by vortex stretching ($-f\nabla \cdot \mathbf{V} > 0$) (Figs. A2f and A3f) associated with this instability of the lower troposphere underneath the Saharan high.

REFERENCES

Arnason, G., 1963: The stability of nongeostrophic perturbations in a baroclinic zonal flow. *Tellus,* **15,** 205–229.

Avila, L. A., and R. J. Pasch, 1992: Atlantic tropical system of 1991. *Mon. Wea. Rev.,* **120,** 2688–2696.

Burpee, R. W., 1972: The origin and structure of easterly waves in the lower troposphere of north Africa. *J. Atmos. Sci.,* **29,** 77–90.

——, 1974: Characteristics of the North African easterly waves during the summers of 1968 and 1969. *J. Atmos. Sci.,* **31,** 1556–1570.

Carlson, T. N., 1969a: Synoptic histories of three African disturbances that developed into Atlantic hurricanes. *Mon. Wea. Rev.,* **97,** 256–276.

——, 1969b: Some remarks on African disturbances and their progress over the tropical Atlantic. *Mon. Wea. Rev.,* **97,** 716–726.

Chang, C. B., 1993: Impact of desert environment on the genesis of African wave disturbances. *J. Atmos. Sci.,* **50,** 2137–2145.

Charney, J. G., and M. E. Stern, 1962: On the stability of internal baroclinic jets in a rotating atmosphere. *J. Atmos. Sci.,* **19,** 159–172.

Chen, T.-C., 2003: Maintenance of summer circulations: A planetary-scale perspective. *J. Climate,* **16,** 2022–2037.

——, 2005: Maintenance of the midtropospheric North African summer circulation: Saharan high and African easterly jet. *J. Climate,* **18,** 2943–2962.

——, and W. E. Baker, 1986: Global diabatic heating during FGGE SOP-1 and SOP-2. *Mon. Wea. Rev.,* **114,** 2578–2589.

Cook, K. H., 1999: Generation of the African easterly jet and its role in determining West African precipitation. *J. Climate,* **12,** 1165–1184.

Eady, E. T., 1949: Long waves and cyclone waves. *Tellus,* **1,** 33–52.

Fink, A. H., D. G. Vincent, P. M. Reiner, and P. Speth, 2004: Mean state and wave disturbances during phase I, II, and III of GATE based on ERA-40. *Mon. Wea. Rev.,* **132,** 1661–1683.

Fjortoft, R., 1950: Application of integral theorems in deriving criteria of stability for laminar flows and for the baroclinic circular vortex. *Geofys. Publ.,* **17** (5), 1–52.

Grist, J. P., 2002: Easterly waves over Africa. Part I: The seasonal cycle and contrasts between wet and dry years. *Mon. Wea. Rev.,* **130,** 197–211.

——, S. E. Nicholson, and A. L. Barcilon, 2002: Easterly wave over Africa. Part II: Observed and modeled contrasts between wet and dry years. *Mon. Wea. Rev.,* **130,** 212–225.

Hodges, K. I., 1995: Feature tracking on the unit sphere. *Mon. Wea. Rev.,* **123,** 3458–3465.

Källberg, P., A. Simmons, S. Uppala, and M. Fuentes, 2004: The ERA-40 archive. ERA-40 Project Report Series 17, 35 pp. [Available online at http://www.ecmwf.int/publications/library/ecpublications/_pdf/era40/ERA40_PRS17.pdf/.]

Kalnay, E., and M. Cai, 2003: Impact of urbanization and land-use change on climate. *Nature,* **423,** 528–531.

Kwon, H. J., 1989: A re-examination of the genesis of African waves. *J. Atmos. Sci.,* **46,** 3621–3631.

Landsea, C. W., 1993: A climatology of intense (or major) Atlantic hurricanes. *Mon. Wea. Rev.,* **121,** 1703–1713.

Lau, K.-H., and N.-G. Lau, 1990: Observed structure and propagation characteristics of tropical summertime synoptic scale disturbances. *Mon. Wea. Rev.,* **118,** 1888–1913.

Lorenz, E. N., 1955: Available potential energy and the maintenance of the general circulation. *Tellus,* **7,** 157–167.

——, 1967: The nature and theory of the general circulation of the atmosphere. WMO 218, Tech. Publication 115, World Meteorological Organization, Geneva, Switzerland, 161 pp.

Mass, C., 1979: A linear primitive equation model of African wave disturbances. *J. Atmos. Sci.,* **36,** 2075–2092.

Murakami, M., 1979: Large-scale aspects of deep convective activity over the GATE area. *Mon. Wea. Rev.,* **107,** 994–1013.

Nicholson, S. E., B. Some, and B. Kone, 2000: A note on the recent rainfall condition in West Africa, including the rainy season of the 1997 ENSO year. *J. Climate,* **13,** 2628–2640.

Nitta, T., and Y. Takayabu, 1985: Global analysis of the lower tropospheric disturbances in the tropics during the northern summer of the FGGE year. Part II: Regional characteristics of the disturbances. *Pure Appl. Geophys.,* **123,** 272–292.

Norquist, D. C., E. E. Recker, and R. J. Reed, 1977: The energetics of African wave disturbances as observed during phase III of GATE. *Mon. Wea. Rev.,* **105,** 334–342.

Pytharoulis, I., and C. Thorncroft, 1999: The low-level structure of African easterly waves in 1995. *Mon. Wea. Rev.,* **127,** 2266–2280.

Reed, R. J., 1979: The structure and behavior of easterly waves over West Africa and the Atlantic. *Meteorology over the Tropical Oceans,* D. B. Show, Ed., Royal Meteorological Society, 57–72.

——, A. Hollingsworth, W. A. Heckley, and F. Delsol, 1988a: An evaluation of the ECMWF operational system in analyzing and forecasting easterly wave disturbances over Africa and the tropical Atlantic. *Mon. Wea. Rev.,* **116,** 824–865.

——, E. Klinker, and A. Hollingsworth, 1988b: The structure and characteristics of African easterly wave disturbances as determined from the ECMWF operational Analysis/Forecast System. *Meteor. Atmos. Phys.,* **38,** 22–33.

Rennick, M. A., 1976: The generation of African waves. *J. Atmos. Sci.,* **33,** 1955–1969.

Sanders, F., 1984: Quasi-geostrophic diagnosis of the monsoon depression of 5-8 July 1979. *J. Atmos. Sci.,* **41,** 538–552.

Simmons, A. J., 1977: A note on the instability of the African easterly jet. *J. Atmos. Sci.,* **34,** 1670–1674.

Thorncroft, C. D., 1995: An idealized study of African easterly waves. Part III: More realistic basic states. *Quart. J. Roy. Meteor. Soc.,* **121,** 1589–1614.

——, and B. J. Hoskins, 1994a: An idealized study of African

easterly waves. Part I: A linear view. *Quart. J. Roy. Meteor. Soc.,* **120,** 953–982.

——, and ——, 1994b: An idealized study of African easterly waves. Part II: A nonlinear view. *Quart. J. Roy. Meteor. Soc.,* **120,** 983–1015.

——, and D. P. Rowell, 1998: Interannual variability of African wave activity in a general circulation model. *Int. J. Climatol.,* **18,** 1305–1323.

——, and K. Hodges, 2001: African easterly wave variability and its relationship to Atlantic tropical cyclone activity. *J. Climate,* **14,** 1166–1179.

van den Hurk, B. J. J. M., P. Viterbo, A. C. M. Beljaars, and A. K. Betts, 2000: Offline validation of the ERA40 surface scheme. ECMWF Tech. Memo. 295, 42 pp.

Wiin-Nielsen, A., and T.-C. Chen, 1993: *Fundamentals of Atmospheric Energetics*. Oxford University Press, 376 pp.